

# Simulated Space Weathering of Fe- and Mg-rich Aqueously Altered Minerals Using Pulsed Laser Irradiation

Kaluna, H. M., Ishii, H. A., Bradley, J. P., Gillis-Davis, J. J., Lucey, P. G.

*Hawaii Institute of Geophysics and Planetology, University of Hawaii, Honolulu-HI-96822*

kaluna@higp.hawaii.edu, hope.ishii@higp.hawaii.edu, jbradley@higp.hawaii.edu,  
gillis-davis@higp.hawaii.edu, lucey@higp.hawaii.edu

## ABSTRACT

Simulated space weathering experiments on volatile-rich carbonaceous chondrites (CCs) have resulted in contrasting spectral behaviors (e.g. reddening vs bluing). The aim of this work is to investigate the origin of these contrasting trends by simulating space weathering on a subset of minerals found in these meteorites. We use pulsed laser irradiation to simulate micrometeorite impacts on aqueously altered minerals and observe their spectral and physical evolution as a function of irradiation time. Irradiation of the mineral lizardite, a Mg-phylosilicate, produces a small degree of reddening and darkening, but a pronounced reduction in band depths with increasing irradiation. In comparison, irradiation of an Fe-rich aqueously altered mineral assemblage composed of cronstedtite, pyrite and siderite, produces significant darkening and band depth suppression. The spectral slopes of the Fe-rich assemblage initially redden then become bluer with increasing irradiation time. Post-irradiation analyses of the Fe-rich assemblage using scanning and transmission electron microscopy reveal the presence of micron sized carbon-rich particles that contain notable fractions of nitrogen and oxygen. Radiative transfer modeling of the Fe-rich assemblage suggests that nanometer sized metallic iron ( $npFe^0$ ) particles result in the initial spectral reddening of the samples, but the increasing production of micron sized carbon particles ( $\mu pC$ ) results in the subsequent spectral bluing. The presence of  $npFe^0$  and the possible catalytic nature of cronstedtite, an Fe-rich phyllosilicate, likely promotes the synthesis of these carbon-rich, organic-like compounds. These experiments indicate that space weathering processes may enable organic synthesis reactions on the surfaces of volatile-rich asteroids. Furthermore, Mg-rich and Fe-rich aqueously altered minerals are dominant at different phases of the aqueous alteration process. Thus, the contrasting spectral slope evolution between the Fe- and Mg-rich samples in these experiments may indicate that space weathering trends of volatile-rich asteroids have a compositional dependency that could be used to determine the aqueous histories of asteroid parent bodies.

*Subject headings:* Asteroids, surfaces; Impact processes; Mineralogy; Spectroscopy; Prebiotic chemistry

## 1. Introduction

Our ability to characterize the composition of Solar System bodies greatly depends on remote sensing data and imaging of spectral features. However, space weathering processes, which alter the surfaces of airless bodies chemically, physically and optically, can introduce spectral variations that reduce our ability to accurately assess the mineralogy of these bodies. Both Solar System bodies that have been sampled by spacecraft, the Moon and the near Earth S-class asteroid

Itokawa, show evidence of space weathering. In particular, the sampled grains from both of these bodies have rims bearing  $npFe^0$  particles, which form in response to processes such as micrometeorite impacts and solar wind sputtering (e.g. Conel & Nash 1970; Keller & McKay 1993; Noguchi et al. 2011). Various types of large, micron-sized glassy agglutinates, which form during micrometeorite bombardment, are also observed in these samples (McKay et al. 1991; Ogliore & Dobrica 2015). Both of these optically active space weathering products result in the reduction

of albedo, increase in spectral slopes (reddening), and the reduction of absorption features with increasing exposure age (see Pieters et al. 2000; Hapke 2001, and references therein).

While the  $npFe^0$  and agglutinates observed in lunar soils and Itokawa samples bear similarities, there are distinct differences in the particles that are attributed to the differing gravities (Ogliore & Dobrica 2015) and compositions of the two bodies. For example, in contrast to lunar soils, a notable fraction of  $npFe^0$  particles are much less abundant on Itokawa and a notable fraction of these particles are sulfur bearing (Noguchi et al. 2011). The differences in these space weathering products may be further amplified in the main asteroid belt, where the reduction in solar wind flux and micrometeorite impact energies (Chapman 2002) may reduce the effectiveness of  $npFe^0$  and agglutinate production. Nonetheless, spectral reddening has been observed among silicate-rich S-complex, and primitive, low-albedo C-complex main belt asteroids (e.g. Jedicke et al. 2004; Nesvorný et al. 2005; Lazzarin et al. 2006; Kaluna et al. 2016b; Fornasier et al. 2016). Although spacecraft have not yet sampled main belt asteroids and we are limited in our understanding of space weathering products on these bodies, meteorites and meteorite analogs provide useful tools that enable the study of space weathering processes through experimentation.

Most published space weathering studies have focused on the spectral evolution of anhydrous minerals found in lunar soils and ordinary chondrites (OC), the meteorite analogs of S-complex asteroids (e.g. Hapke 1966; Yamada et al. 1999; Sasaki et al. 2001). In contrast, the number of experiments on CC meteorites is relatively small (Table 1) compared to the large compositional diversity of CC meteorites (Burbine et al. 2002). Ion or pulsed laser irradiation of some CCs results in the reddening and darkening of meteorite spectra similar to the optical variations observed among experimentally space weathered OCs. However, experiments on the aqueously altered CC meteorites Tagish Lake, Mighei and Murchison reveal a new trend of decreased spectral slopes (i.e. flattening or bluing) with increased exposure to ion bombardment or laser irradiation (Hiroi et al. 2004; Vernazza et al. 2013; Matsuoka et al. 2015; Lantz et al. 2015b).

In comparison, both reddening and bluing trends have been observed among C-complex asteroids. However, Lazzarin et al. (2006) and Kaluna et al. (2016b) suggest the bluing trend found by Nesvorný

et al. (2005) arises from compositional variations rather than space weathering processes. Observations of the C-complex, Themis asteroid family and its younger sub-family, the Beagle asteroids, show spectral reddening with increasing age (Kaluna et al. 2016b; Fornasier et al. 2016). Due to their common origin (Hirayama 1918; Nesvorný et al. 2008) and similarity in spectral features (Kaluna 2015; Kaluna et al. 2016a), the observed spectral reddening among these two families is unlikely the result of compositional heterogeneity (Kaluna et al. 2016b). Though the Themis and Beagle asteroid families provide a useful tool to study space weathering, they are currently the only known C-complex asteroids that originate from the same parent body while having different dynamical (i.e. surface) ages. Thus, the bluing observed in simulated space weathering experiments may still be representative of space weathering trends on other C-complex asteroid families.

The volatile-rich CI and CM meteorites contain a significant fraction of phyllosilicates (up to 80 wt.% Cloutis et al. (2011)), which are the group of minerals associated with the spectral features in C-complex asteroids (e.g. Lebofsky et al. 1981; Vilas & Gaffey 1989). Modal mineralogy of volatile-rich CCs suggests that Fe-rich phyllosilicates give way to Mg-rich end members as aqueous alteration progresses (Howard et al. 2009, 2011; Rubin 2007). In this study, we have selected a subset of the minerals and assemblages that are representative of these two end phases of aqueous alteration to investigate the role these minerals have on the space weathering trends of volatile-rich CCs and C-complex asteroids. We performed pulsed-laser irradiation on the Mg-rich phyllosilicate lizardite and an Fe-rich assemblage consisting of cronstedtite, pyrite and siderite to simulate the effects of micrometeorite impacts. The same experimental procedure was used with San Carlos olivine to compare the spectral trends of our aqueously altered samples with those of lunar and S-type mineralogies.

## 2. Methodology

### 2.1. Sample characterization and preparation

For this study we irradiated two sets of aqueously altered terrestrial minerals, the Mg-rich phyllosilicate lizardite ( $Mg_3(Si_2O_5)(OH)_4$ ), and an Fe-rich assemblage composed of cronstedtite ( $Fe^{2+}_2Fe^{3+}(SiFe^{3+})O_5(OH)_4$ ), pyrite ( $FeS_2$ ) and siderite ( $FeCO_3$ ). The lizardite was manually extracted from an assemblage where

lizardite sheets were interspersed with artinite ( $\text{Mg}_2(\text{CO}_3)(\text{OH})_2 \cdot 3\text{H}_2\text{O}$ ) and siderite. The Fe-rich assemblage, which occurred as siderite and pyrite crystals embedded in a cronstedtite matrix, was isolated from a basalt-like host rock using a rotary tool and diamond tipped bits.

Chemical compositions of lizardite and Fe-rich assemblage thin sections were determined using the Hawaii Institute of Geophysics and Planetology's (HIGP) electron microprobe. The electron microprobe is a JEOL JXA-8500F field-emission gun microanalyzer with 5 wavelength-dispersive spectrometers. Beam currents of 4.0 nA for lizardite and 5.0 nA for the Fe-rich assemblage were used with a spot size of  $10\mu\text{m}$  for both samples. For the Fe-rich assemblage, Fe-olivine was used as a mineral standard for Si, San Carlos olivine for Mg, anorthite for Al, and troilite for Fe and S with errors of  $\sim 1\%$ . The mineral standards used for lizardite were San Carlos olivine for Si, Fe and Mg, and plagioclase for Al, with errors of ranging from  $\sim 0.3\text{-}7\%$ . A secondary electron (SE) image of the cronstedtite, pyrite and siderite phases in the Fe-rich assemblage is shown in Figure 1. Reactions near the pyrite and cronstedtite interfaces have oxidized some of the pyrite, resulting in leached sulfur and an enrichment in iron and oxygen. The fractional abundances for lizardite and each of the phases in the Fe-rich assemblage are given in Table 2.

To determine the modal mineralogy of the samples, we used x-ray diffraction. Powdered samples were measured using the HIGP's InXitu Inc. X-ray diffraction / X-ray fluorescence (XRD/XRF) instrument. The XRD analysis revealed that the lizardite sample was pure and the Fe-rich assemblage was composed of  $\sim 73\text{ wt.}\%$  cronstedtite,  $23\text{ wt.}\%$  pyrite and  $3\text{ wt.}\%$  siderite.

## 2.2. Experimental procedure

The powdered samples were dry-sieved into size fractions greater and less than  $75\mu\text{m}$ . The laser irradiation experiments utilized  $\sim 0.5$  gram of each sample from the  $<75\mu\text{m}$  size fraction powders, which were placed into a glass beaker as a loose powder. To simulate space weathering by  $1\mu\text{m}$  dust impacts with velocities typical at 1 AU, we used a pulsed laser with a focused spot size of  $\sim 0.25\text{ mm}$ , a pulse energy of 30 mJ (Sasaki et al. 2001, 2003) and pulse duration of 6-8 nanoseconds. The pulse duration is similar to the timescale of micrometeorite dust impacts (Yamada et al. 1999). The samples were irradiated under vacuum at pressures of  $10^{-5}$  to  $10^{-6}$  mbar with a Contin-

uum Surelite-I-20 Nd:YAG 1064 nm laser pulsed at a frequency of 20 Hz. A manually adjusted pan/tilt mirror was used to move the laser spot and irradiate the full area of the sample. The incident laser gardened the samples vertically during irradiation, leading to uniform simulated weathering.

Three sets of experiments were conducted on each sample to quantify variability in the space weathering trends. Each of the samples were irradiated multiple times over a consistent set of intervals in order to monitor the spectral evolution of the samples as a function of irradiation time. The lizardite and olivine samples were irradiated at intervals of 2.5, 2.5, 5.0, 5.0, 5.0, 10.0, 10.0, 10.0 and 10.0 minutes for a total of 60 minutes. The irradiation intervals for Fe-rich assemblage followed the same interval sequence as olivine and lizardite, however the sequence was halted at 40 minutes. We were forced to shorten the irradiation sequence due to the considerable volatility of the Fe-rich samples in response to the laser, which resulted in a notable portion of the samples being displaced from the glass beakers into the vacuum chamber. Gas partial pressures of water and other volatiles released during irradiation were monitored using a 100amu Residual Gas Analyzer (RGA) from Stanford Research System. The RGA is attached to the vacuum chamber, and uses an ionizer and a quadrapole mass filter to measure volatiles released as a function of atomic mass.

Spectral data were obtained using a visible and near-infrared wavelength ( $0.35\text{-}2.5\mu\text{m}$ ) FieldSpec 4 Spectroradiometer from Analytical Spectral Devices Inc. The spectroradiometer has resolutions of 3 nm and 10 nm in the  $0.35\text{-}1.0\mu\text{m}$  and the  $1.0\text{-}2.5\mu\text{m}$  regions, respectively. The reflectance spectra were measured relative to a 99% reflectance LabSphere Spectralon Standard and taken at incidence and emission angles of  $i=30^\circ$  and  $e=0^\circ$ . The spectral measurements were conducted outside of the vacuum chamber and made after each irradiation interval. Samples were prepared for spectral measurements by placing them in a sample holder and leveling the sample surface by moving a flat spatula across the top of the holder, taking care not to compress the sample. Spectra were taken at four positions on the sample, after which the sample was removed, mixed and placed back into the holder, and the sequence repeated twice more. This process results in 12 spectra that account for packing effects and sample variability during placement into the holder.

### 2.3. Post-irradiation sample characterization

To characterize the irradiation products of the lizardite and Fe-rich assemblage samples, we obtained nanometer scale, high resolution images using the Pacific Biosciences Research Center's (PBRC) Hitachi S-4800 field emission scanning electron microscope (SEM). SE images were taken of a 60-minute irradiated lizardite sample and a 40-minute irradiated Fe-rich assemblage. Prior to imaging, the irradiated mineral grains were mounted onto sample stubs with double sided carbon tape. The SE images of lizardite were obtained using a current of 5kV and acceleration voltages of 6.2-10.9 $\mu$ A, whereas a configuration of 2kV and 8.6-16.8 $\mu$ m was used for the Fe-rich assemblage.

Two melt grains from the irradiated Fe-rich samples were selected for further characterization and made into Focused Ion Beam (FIB) sections for analysis with transmission electron microscopy (TEM). The first grain was cut and prepared using an FEI Strata 235 dual beam FIB at the Molecular Foundry, Lawrence Berkeley Lab. The second FIB section was prepared with the FEI Helios 650 dual beam FIB at Oregon State University's Electron Microscopy Facility. A focused Ga<sup>+</sup> ion beam was used for site-selective extraction of laser-irradiated grain sections and were attached to Cu half-grids for subsequent TEM analyses. Field emission SE and secondary ion images were obtained of the FIB sections during sample preparation, and standard FIB sample preparation procedures were applied with final thinning of the sections on the TEM grid (e.g. Ishii et al. 2010).

The Fe-rich assemblage FIB sections were analyzed by scanning transmission electron microscopy on two FEI Titan (S)TEMs. One microscope is a 80-200 kV Titan at Oregon State University (OSU), and the other is a 60-300kV Titan (referred to as TitanX) at the National Center for Electron Microscopy (NCEM), Molecular Foundry, Lawrence Berkeley Lab. Each instrument has a high brightness FEG and ChemiSTEM technology consisting of four Bruker silicon drift detectors (SDDs) for 0.7 sr total solid angle acceptance and 140 eV energy resolution at Mn K-alpha. Energy dispersive x-ray (EDX) mapping on all FIB sections was carried out with 10 eV/pixel dispersion. The convergence semi-angle alpha was 10.0 mrad on both instruments, and the HAADF inner semi-angle beta was set at 40 mrad at OSU and 63 mrad at NCEM. EDX mapping on the first FIB section was carried out on the OSU Titan at 200 kV and 400 pA with pixels of 6

nm on a side, 998 pixels width and 662 pixels height, with a total collection time of 4.3 ms/pixel. Full x-ray fluorescence spectra were collected at each pixel, however due to its superior low-energy performance, additional chemical analyses were carried out on the NCEM TitanX. EDX mapping on the second FIB section was also conducted with the NCEM TitanX using 200kV and full x-ray fluorescence spectra collected at each pixel. The map was carried out at 900 pA beam current with pixels of 9.3 nm on a side, 352 pixels wide and 292 pixels high, with a total collection time of 8.2 ms/pixel. Maps were processed using Bruker's Esprit 1.9 analysis software, and regions of interest within the FIB sections were drawn and spectra from pixels within those regions summed, fitted and quantified to obtain chemical compositions.

### 2.4. Radiative Transfer Modeling

We used a modification of the Hapke (2001) radiative transfer model from Lucey & Riner (2011) to estimate the abundance and model the optical effects of nanophase and microphase metallic iron particles ( $npFe^0$  and  $\mu pFe^0$ , respectively) on the irradiated sample spectra of olivine, lizardite and the Fe-rich assemblage samples. The model uses Mie theory to look at the effects of reddening and darkening from nanophase particles ( $< 50$  nm), in addition to the purely darkening effect of microphase particles ( $> 50$  nm). SEM imaging and TEM analysis revealed the presence of micron sized carbon particles on the irradiated Fe-rich sample grains, so we also modeled the effects of nanophase and microphase amorphous carbon ( $npC$  and  $\mu pC$  respectively) particles in addition to  $npFe^0$  and  $\mu pFe^0$  for the Fe-rich samples.

The spectra and associated viewing geometry ( $i=30^\circ$  and  $e=0^\circ$ ) of our fresh (non-irradiated) samples are used as input into the model, along with the mean grain diameters (37.5 $\mu$ m), grain densities ( $\rho_{olivine} = 3.32\text{g/cm}^3$ ,  $\rho_{lizardite} = 2.55\text{g/cm}^3$  and  $\rho_{Fe-rich} = 3.34\text{g/cm}^3$ ) and real indices of refraction ( $n_{olivine} = 1.64$ ,  $n_{lizardite} = 1.60$  and  $n_{Fe-rich} = 1.72$ ). Because it is the most abundant mineral in the sample, we use the real index of refraction and density of cronstedtite as input into the model for the Fe-rich assemblage. The optical constants used in our models are derived from Cahill et al. (2012) for iron and Rouleau & Martin (1991) for the amorphous carbon.

These initial parameters are first used to obtain the complex index of refraction spectrum for each sam-



ple, which is then used along with estimated values of the nanophase and microphase particle abundances to derive a modeled irradiated spectrum. For each spectrum, we use the IDL routine MPFIT (Markwardt 2009), to vary the input abundances and perform a non-linear least squares fit between our model and the observed spectrum. This allows us to derive robust model spectra and particle abundances for each sample as a function of laser irradiation time.

### 3. Results

#### 3.1. Spectroscopic Trends

Spectra of olivine, lizardite and the Fe-rich assemblage as a function of irradiation time are shown in Fig. 2. Although we use loosely packed powders in our experiments, our irradiated olivine shows a similar increase in spectral slope, and decrease in reflectance (i.e. albedo) and band depth when compared to other studies that use compressed pellets (e.g Yamada et al. 1999; Brunetto & Strazzulla 2005). Figure 2 reveals that both the lizardite and Fe-rich samples exhibit irradiation dependent spectral variations. A comparison of the relative (data were normalized to the initial value in each experiment) albedo and slope variations of all samples is given in Fig. 3.

Albedo and slope were defined by using visible and near-infrared (near-IR) continuum points not affected by absorption features. Thus, due to the difference in mineral features, the wavelengths of the continuum points used in our analysis are different for each sample. The reflectance values at  $0.70\ \mu\text{m}$  were used to measure the visible region albedo variations in olivine, and values at  $0.57\ \mu\text{m}$  and  $0.60\ \mu\text{m}$  were used for lizardite and the Fe-rich assemblage, respectively. For the near-IR albedo variations, reflectance values at  $2.30\ \mu\text{m}$  for olivine,  $2.16\ \mu\text{m}$  for lizardite, and  $2.20\ \mu\text{m}$  for the Fe-rich assemblage were used.

The wavelength value of  $0.55\ \mu\text{m}$  is often used to scale reflectance spectra in both experimental and observational data (e.g. Sasaki et al. 2001; Bus & Binzel 2002; Fornasier et al. 2014), so for consistency and to allow for comparison with other works, we used reflectance values at  $0.55\ \mu\text{m}$  to characterize slope variations in our sample spectra. Due to broad absorption features and the lack of extended continuum regions in the visible, the visible slopes for these minerals were measured using one point in the visible and the other in the near-IR. A linear fit to the normalized reflectance values at  $0.70\ \mu\text{m}$  and  $1.60\ \mu\text{m}$  were

used to characterize visible slope variations for olivine, and  $0.57\ \mu\text{m}$  and  $1.70\ \mu\text{m}$  were used for lizardite. In contrast to the other minerals, the Fe-rich assemblage has an extended continuum region in the visible, so slope variations were measured using a linear fit to continuum points at  $0.60\ \mu\text{m}$  and  $0.75\ \mu\text{m}$ . For the near-IR region, slopes were computed using normalized reflectance values at  $1.60\ \mu\text{m}$  and  $2.30\ \mu\text{m}$  for olivine, and at  $1.70\ \mu\text{m}$  and  $2.16\ \mu\text{m}$  for lizardite. The Fe-rich assemblage has only one continuum point in the near-IR because of absorption features, so near-IR slopes were measured using one point in the visible ( $0.75\ \mu\text{m}$ ) and one point in the near-IR ( $2.20\ \mu\text{m}$ ).

Figure 3 reveals that the evolution of spectral slopes is related to the wavelength dependency of the albedo variations. For instance, the reduction of albedo in olivine is greatest at shorter wavelengths, resulting in an increase of spectral slopes (reddening). Lizardite shows a slight decrease in albedo at visible wavelengths, but no variations in the near-IR, resulting in a slight reddening as a function of irradiation time. Although the variations are much smaller, the spectral behavior of lizardite is similar to olivine, and is consistent with the production of  $np\text{Fe}^0$  particles, which induce spectral reddening due to a decrease in the absorption efficiency of the  $np\text{Fe}^0$  coated grains at longer wavelengths Hapke (2001).

In contrast to olivine and lizardite, the slopes of the Fe-rich assemblage samples initially redden, then reverse and become bluer with increased irradiation. As seen in Figure 3, the albedo of the Fe-rich assemblage initially decreases more rapidly at visible wavelengths than in the near-IR, but eventually begins to plateau while the near-IR albedo continues to decrease. This relative difference in the visible and near-IR albedo trends results in the reversal from slope reddening to bluing. Our proposed hypothesis for the cause of the spectral bluing is described in the following sections.

Band depth measurements for olivine and lizardite were made after dividing the full spectrum by a linear fit to the continuum shoulders on either side of an absorption feature. The band depths for the broad  $\text{Fe}^{2+}$  feature centered at  $1.05\ \mu\text{m}$  in olivine were derived using continuum points at  $0.70\ \mu\text{m}$  and  $1.60\ \mu\text{m}$ . Although the Fe-rich assemblage exhibits a broad feature between  $\sim 0.7$  to  $2.0\ \mu\text{m}$ , the lack of clear shoulders and minima made characterization in this region difficult. Thus, we use the feature near  $2.4\ \mu\text{m}$  to characterize the band depth changes as a function of irradiation time. However, due to the presence of only one

continuum shoulder, we were limited to using a ratio of the reflectance values near the band minimum and shoulder at  $2.4\ \mu\text{m}$  and  $2.2\ \mu\text{m}$ , respectively. Measurements of the lizardite  $\text{Fe}^{2+} \rightarrow \text{Fe}^{3+}$  minima at 0.75, 0.92, and  $1.13\ \mu\text{m}$  (Burns 1993) were measured using the continuum shoulders at  $0.57\ \mu\text{m}$  and  $1.7\ \mu\text{m}$ . Figure 4a shows the relative variations in the olivine  $1.05\ \mu\text{m}$ , lizardite  $1.13\ \mu\text{m}$  and the Fe-rich assemblage  $2.4\ \mu\text{m}$  features. It is important to note that while band depths variations were observed, no significant variations were seen in the absorption band center wavelengths. Although the slope and albedo variations are quite different for each of the samples, the Fe-rich assemblage, lizardite and olivine all show similar trends in band depth reduction.

In addition to the  $\text{Fe}^{2+} \rightarrow \text{Fe}^{3+}$  intervalence charge transfer (IVCT) features, lizardite also has a suite of absorption features caused by hydroxyl overtones (Calvin & King 1997) and water (Jain et al. 2012). The multiple spectral features provide a useful tool to characterize how each of these species varies in response to simulated space weathering. Variations in the OH band depths were measured using continuum shoulders near  $1.35\ \mu\text{m}$  and  $1.45\ \mu\text{m}$  for the  $1.4\ \mu\text{m}$  feature, and  $2.28\ \mu\text{m}$  and  $2.35\ \mu\text{m}$  for the  $2.3\ \mu\text{m}$  feature.  $\text{H}_2\text{O}$  features at  $1.98\ \mu\text{m}$  and  $2.13\ \mu\text{m}$  were characterized using continuum shoulders near  $1.85\ \mu\text{m}$  and  $2.2\ \mu\text{m}$ . Figure 4b compares the relative reduction in band depths between each of the lizardite IVCT, hydroxyl and water features measured in this study. The iron features exhibit the greatest band reduction, while the hydroxyl features are the least affected by laser irradiation. Additionally, the degree of band reduction for all three species decreases at longer wavelengths. This wavelength dependency on band reduction is consistent with the production of  $\text{npFe}^0$ , however it appears that  $\text{npFe}^0$  does not affect all features equally and a compositional dependency also exists.

### 3.2. Volatile Production

Partial pressure measurements for a variety of gases ( $\text{H}_2\text{O}$ ,  $\text{N}_2$ ,  $\text{CO}$ ,  $\text{CO}_2$ ) released during 5-minute laser irradiation series of olivine, lizardite and the Fe-rich assemblage are shown in Fig. 5a-c. When comparing the fluctuations as a function of irradiation time, the similarity in fluctuations between the gases and nitrogen suggest the majority of the species originate from air trapped in the sample powders. It is also evident that the samples appear to trap and release different fractions of air during irradiation, suggesting that the

‘trapping’ efficiency is different from mineral to mineral.

$\text{H}_2\text{O}$  was detected during the irradiation of olivine but occurs at levels an order of magnitude less than the other minerals and likely originates from adsorbed water. A significant fraction of  $\text{H}_2\text{O}$  was released from the aqueously altered minerals, which decreases from the initial to final experiments by  $\sim 30\%$  for lizardite and  $\sim 50\%$  for the Fe-rich assemblage. Reflectance spectra also show a similar degree of reduction in  $\text{H}_2\text{O}$  band depths, with lizardite showing a band reduction of  $\sim 20\%$  and the Fe-rich assemblage showing a reduction of  $\sim 60\%$ . While there is some consistency between the fraction of  $\text{H}_2\text{O}$  released and the band depth variations, it is important to note that there is also a wide spread in the partial pressure values across the three experiments for each irradiation sequence (Fig. 5d). These large standard deviations likely arise from variations in the fraction of water that is re-adsorbed by the samples when they are taken out of the vacuum chamber for spectral imaging, however quantifying the fraction of the native versus adsorbed water lost during the irradiation is beyond the scope of this study. Nevertheless, in contrast to previous interpretations (e.g. Rivkin et al. 2002), these data show that the liberation of water and the creation of  $\text{npFe}^0$  and other space weathering products can occur in conjunction. In other words, the samples do not have to be dehydrated before the creation of  $\text{npFe}^0$  can occur.

### 3.3. SEM and TEM sample characterization

SE images of the 60 minute irradiated lizardite and 40 minute irradiated Fe-rich assemblage grains both show widespread melt deposition, however, there is a distinct difference in the physical appearance of the two samples (Fig. 6a-d). Particularly noticeable in Fig. 6a and 6b are very fine lizardite needles, only a few microns in length, coating the melt deposition regions on the larger host grain. Due to the fibrous nature of lizardite, these needles are likely remaining pieces of the irradiated portion of the sample that re-deposited on nearby grains. These fine fibers appear to be covering a significant fraction of the melt deposits and may be impeding the optical effects of  $\text{npFe}^0$  on the spectral features of the lizardite samples. In particular, the contrasting behavior between the significant reduction in the  $\text{Fe}^{2+} \rightarrow \text{Fe}^{3+}$  IVCT band depths and the minimal changes in albedo and slope may be a result of the fibers preferentially reducing some optical properties of  $\text{npFe}^0$  over others.

Figures 6d and 7 show two characteristic types of deposition materials observed through the Fe-rich samples. The first type (Fig. 6d) resemble the melt deposits seen on the lizardite grains, whereas the second type (Fig. 7) consists of larger, micron sized dark particles. Element maps of the first FIB section (FIB section 1) taken with the OSU Titan (Fig. 8) show that the dark grain is a large carbon-rich particle coated by a thin layer of Fe, O and Si. The Pt and Ga map represents regions to ignore as this is where sputtering during the ion milling process leads to the redeposition of Pt, Ga and bulk sample atoms in void spaces. Adjacent to the C grain are two small, Fe rich melt droplets that contain Si, O, and S (Table 3). Unexpectedly, EDX analysis of the C-rich region reveal the presence of nitrogen. To confirm the nitrogen signature, EDX analysis was repeated on the C-grain using the superior NCEM TitanX. Both analyses are given in Table 3, and while the first analysis detected small amounts of Si and Fe, it is likely from the redeposition of FIB sputtered material in a narrow void region. The second analysis shows that the grain is purely composed of C, N and O when the void region is excluded. These results suggest the grain may be some form of an organic compound or a synthesized heterofullerene.

Elemental maps of the second FIB section (FIB section 2) are shown in Figure 9. To assess whether the nitrogen content in the FIB section 1 was anomalous, EDX analysis was performed on FIB section 2 with the NCEM TitanX. Again nitrogen was found in the C-rich region of the grain (Tab. 3), suggesting that N may be common among these dark particles. The semi-continuous glassy rim surrounding the C-rich grain was found to contain oxidized rather than metallic Fe. The Fe particles were likely oxidized during irradiation, however there remains the possibility that oxidation occurred when the samples were removed from the vacuum chamber, or after sample processing by FIB. Analyses of a relatively large ( $\sim 50\text{nm}$ ) droplet in the rim was found to contain C, N, O, Fe, and S. The presence of N in the melt rim of the FIB section 2 (Tab. 3) as well as the carbon grains show that the nitrogen content is not anomalous and likely common throughout the laser-irradiated samples. Data collected with the RGA show the release of atmospheric species (e.g. N and O) from our samples during irradiation, thus the nitrogen in these grains likely comes from reactions with the local atmosphere created during irradiation.

### 3.4. Radiative Transfer Model Abundances

The modified Hapke modeling allows us to study not only the optical effects of the nanophase and microphase particles, but also the evolution of and relationship between these particles. Figure 10 shows the best fit radiative transfer models for the initial and final irradiated spectra for each sample. Although both  $np\text{Fe}^0$  and  $\mu p\text{Fe}^0$  were considered in the model inputs, the addition of  $\mu p\text{Fe}^0$  did not improve the fits for the olivine and lizardite spectra. The best fit model abundances for each sample spectrum as a function of irradiation time are given in Table 4. As is evident from Fig. 10b, the model does a poor job of reproducing the 40 minute (total) irradiated lizardite spectrum. The SEM images of lizardite (Fig. 6) revealed that the melt deposits were partially coated in very fine lizardite needles. The poor fits of our model may result from the potential effect of these needles on the effects of  $np\text{Fe}^0$  or the limitations of our model, which assumes spherical host grains and nanoparticles. Thus, the  $np\text{Fe}^0$  abundances in Table 4 are simply used as broad approximations for the production of  $np\text{Fe}^0$  during irradiation.

Due to the presence of micron sized carbon particles, the Fe-rich assemblage models consider the optical effects of both iron and carbon particles (Fig. 10c). We find that models using only  $np\text{Fe}^0$  particles reproduce the spectral reddening reasonably well, but do a poor job of reproducing the spectral variations once bluing occurs. The addition of  $\mu p\text{Fe}^0$  improves the model fits, however we find the best spectral fits are obtained using a combination of  $np\text{Fe}^0$  and  $\mu p\text{C}$  particles. Some  $np\text{C}$  particles were observed in the rim of one dark melt grain, however these particles do not improve the model fits, which may suggest that the carbon particles are typically larger, micron sized particles. Our best fit models show that  $np\text{Fe}^0$  is the dominant particle produced during the initial set of irradiation sequences and corresponds to the initial spectral reddening of the samples. The models also show that  $\mu p\text{C}$  particles quickly become more abundant beyond  $\sim 15$  minutes of irradiation, which coincides with the observed spectral bluing. Thus, our models suggest that the  $np\text{Fe}^0$  particles produce the observed spectral reddening whereas the  $\mu p\text{C}$  particles are largely responsible for the spectral bluing in our Fe-rich samples.

It is important to note that while the best fit models show an increase in the fraction of  $np\text{Fe}^0$  and  $\mu p\text{C}$  with

increasing irradiation time, the abundances of  $npFe^0$  begins to decrease beyond  $\sim 15$  minutes and reduces to zero for the final irradiated spectrum (Table 4). This peculiar trend may result from the  $\mu pC$  particles dominating the optical properties of the sample once a critical abundance is reached, but it may also be a product of using Hapke's model, which was designed for use with transparent materials, on opaque minerals. However, while our results may be further improved by using a more complex radiative transfer model, the models presented here are able to reproduce the spectral variations of our Fe-rich samples reasonably well. So although the modeled  $npFe^0$  and  $\mu pC$  abundances may not reflect the true abundances in our samples, our results still provide values insights into the relative role that these particles play in the spectral behavior of our samples.

## 4. Discussion

### 4.1. Abiotic organic synthesis resulting from space weathering

Although airless bodies are exposed to the harsh environment of space, impacts, cosmic radiation and other space weathering processes supply a source of energy that can be used to drive chemical reactions on the surfaces of these bodies. Of particular interest is the synthesis of organic compounds on extraterrestrial bodies as they may play an important role in the delivery of prebiotic material to the early Earth (Chyba & Sagan 1992). Initial experiments simulating the evolution of organic molecules used ion bombardment of carbon-containing ices and hydrocarbon species to form complex organic compounds (e.g Foti et al. 1984; Johnson et al. 1984; Strazzulla & Johnson 1991; McDonald et al. 1996).

Laboratory VUV radiation experiments conducted on simple organic compounds in the presence of montmorillonite, kaolinite and volcanic ash yield 2-3 times more complex compounds than experiments without a mineral substrate (Simakov & Kuzicheva 2005). Thus, while most ion bombardment experiments are typically conducted without the use of mineral substrates, they may limit carbonization processes by trapping and protecting newly formed compounds from photolysis (Bonner et al. 1985; Simakov & Kuzicheva 2005). The increasing abundance of micron sized carbon particles with increasing irradiation time, as indicated by our modeling and SEM imaging, suggests these particles are being synthesized during the pulsed laser irra-

diation of the Fe-rich sample and are not simply contamination products. Even if the micron sized carbon grains in our irradiated Fe-rich samples are inorganic, these carbon rich grains have not been observed in previous space weathering experiments. Thus, the formation of these particles may be supported by the catalytic properties of cronstedtite in addition to those of  $npFe^0$  particles (Britt et al. 2014).

Most organic irradiation experiments study the evolution of simple carbon species and/or organic-rich compounds that progress towards more complex organics, but as of yet, the production of organics from refractory materials has not been observed. Although we cannot yet rule out the possibility of having synthesized some inorganic form of carbon, the following discussion examines the viability of organic synthesis in response to pulsed laser irradiation and its implications for the production of organics on the surfaces of asteroids.

Industrial Fischer-Tropsch (FT) type reactions commonly use iron oxides and metallic iron as catalysts for organic synthesis (e.g. hydrocarbon fuels) de Smit & Weckhuysen (2008); Britt et al. (2014). In its simplest form, FT reactions combine CO and  $H_2$  to form hydrocarbons and water, e.g. Eq. 1



The production of  $npFe$  (be it metallic or oxidized) from the pulsed laser irradiation of our Fe-rich samples may provide a catalytic source for organic synthesis during our experiments. Additionally, studies on the thermodynamic properties of siderite show that for a range of pressures and temperatures, siderite decomposes to magnetite, graphite and  $CO_2$  before melting (Kang et al. 2015). Although our experiments are conducted at pressures much lower than the studies of Kang et al. (2015), we postulate that a similar type of decomposition produces feedstock carbon species during the irradiation of siderite. Lastly, because our samples are not pressed into pellets (to better simulate asteroid-like regoliths), air trapped in our samples provide a source of N that would otherwise not be readily available in prior experiments. Thus, the presence of C, Fe-oxides (and/or Fe-metals),  $H_2O$  and N provide the Fe-rich samples with an ample set of feedstock minerals and volatiles to potentially enable organic synthesis.

Recent observations of ammoniated clays on Ceres (de Sanctis et al. 2015) and ammonia contained within CCs (Pizzarello & Williams 2012) suggest aster-

oids have notable reservoirs of N-bearing feedstock volatiles that are available for organic synthesis. Additional analyses are currently being conducted to better assess the nature of the micron sized carbon particles in our samples. These particles may represent the first step in a series of reactions that lead to complex, biologically significant organic compounds on the surfaces of asteroids (Britt et al. 2014).

#### 4.2. Comparison to space weathering experiments on meteorites

The spectral bluing observed in this study appears to result from the production of large, micron sized organic-like particles, however, previous studies have found several other mechanisms that result in spectral bluing. In particular, Moroz et al. (1998) and Moroz et al. (2004a) find that ion bombardment of pure complex organics results in spectral bluing due to brightening at UV wavelengths. Moroz et al. (2004a) conclude that the brightening in these experiments results from carbonization, which increases the absorption coefficients and optical density of organics. Similar to the behavior of irradiated organics, both ion bombardment and pulsed-laser irradiation experiments on the meteorites Tagish Lake and Mighei produce flatter spectra (bluing) and brightening at UV wavelengths (Table 1). Thus, the bluing of these meteorites is largely attributed to the carbonization of organics (Hiroi et al. 2004; Vernazza et al. 2013; Lantz et al. 2015a).

Matsuoka et al. (2015) also observes brightening and bluing of laser irradiated Murchison, but in addition to carbonization, they propose that the 10-1000nm Fe and S-rich vapor deposits also contribute to bluing. In contrast, nanophase FeS particles are present in Itokawa samples (Noguchi et al. 2011), and space weathering trends on this asteroid show spectral reddening (Ishiguro et al. 2007). EDX analysis of our irradiated Fe-rich samples revealed small amounts of sulfur associated with the  $npFe^0$  in the rims surrounding the carbon-rich melt grains. The initial spectral reddening of the Fe-rich samples was only reproducible in our radiative transfer models through the use of  $npFe^0$  particles. Thus, just as Keller et al. (2013) postulated, we conclude that nanophase FeS particles likely have analogous optical effects as  $npFe^0$  particles.

Although the  $npFeS$  particles likely cause spectral reddening, another possible mechanism for spectral bluing may arise from larger Fe- and/or FeS-rich particles. In addition to the  $\mu pC$  particles,  $\sim 30$ -50 nm

sized Fe and S-rich melt particles were observed in the irradiated Fe-rich samples. Although our radiative transfer models did not consider sulfur particles, the models that combine both small and large Fe particles ( $npFe^0$  and  $\mu pFe^0$ ) produce similar, albeit poorer fits to the final irradiated Fe-rich sample spectra as the best fit  $npFe^0$  and  $\mu pC$  models. Thus, assuming that these larger particles behave similar to the modeled  $\mu pFe^0$  particles, Fe and S-rich particles may also contribute to the bluing effect observed in our samples. Nonetheless, our TEM data and radiative transfer models suggest that the  $\mu pC$  particles are an important and dominant irradiation product in this study.

#### 4.3. Comparison to space weathering trends on volatile-rich asteroids

The production of micron sized carbon grains has not yet been observed in other experiments, but presents a new mechanism for bluing that may have important implications regarding the spectral trends of asteroids. However, to date astronomical observations have predominantly shown that volatile-rich asteroids experience spectral reddening as a function of exposure age (Lazzarin et al. 2006; Kaluna et al. 2016b; Fornasier et al. 2016; Jaumann et al. 2016). High resolution images of Ceres obtained with the Dawn spacecraft (Russell & Raymond 2011) show a progression from young, blue impact craters to redder, older surface regions (Jaumann et al. 2016). Ceres's mineralogy is dominated by Mg-rich serpentines and carbonates (de Sanctis et al. 2015; Ammannito et al. 2016), which is an indicator that the aqueous alteration on Ceres was progressive (Howard et al. 2009, 2011; Rubin 2007). The spectral reddening observed in our Mg-rich lizardite samples are consistent with the space weathering trends observed on Ceres, and may indicate Mg-rich clays dominate the space weathering trends of this dwarf planet. Similar to Ceres, the C-complex Themis and Beagle asteroid families show a progression towards spectrally redder surfaces with increasing exposure age (Kaluna et al. 2016b; Fornasier et al. 2016), which may indicate that these asteroids are dominated by Mg-rich phyllosilicates. Although Dawn data shows evidence of extensive aqueous alteration, water ice and sublimation activity has also been detected on Ceres (Küppers et al. 2014; Combe et al. 2016). Interestingly, the Themis and Beagle families are also associated with ice in the form of main-belt comets (e.g. Hsieh 2009; Novaković et al. 2012). This is further evidence of the similarities between Ceres

and the Themis and Beagle asteroids, and indicates that prior to its disruption, the Themis/Beagle parent body may have had a similar composition and aqueous history as Ceres.

While spectral reddening have been observed on Themis, Beagle and Ceres, these trends may not be representative of those that occur on other volatile-rich asteroids. Noguchi et al. (2016) find that organics are lost with more pervasive aqueous alteration, and thus bluing trends induced by carbonization may be associated with less altered C-complex asteroids. The Fe-rich sample used in this study is dominated by Fe-rich mineral cronstedtite, which is one of the dominant phyllosilicates formed during the early stages of aqueous alteration (Howard et al. 2009, 2011; Rubin 2007). Thus, the spectral bluing trends of this sample may be representative of asteroids that have experienced small degrees of alteration. Additionally, Lantz et al. (2015b) found a broad correlation between the spectral evolution of meteorites and their initial albedos and possibly carbon content. While a much larger set of experiments are still needed to constrain the spectral trends of volatile-rich CCs, the data presented here along with the Lantz et al. (2015b) study appear to indicate that the compositional dependency of space weathering trends may be a useful tool to constrain the compositions and aqueous histories of volatile-rich asteroids. An example of an asteroid family that may be inclined towards spectral bluing are the Veritas asteroids. This family is noted for pervasive  $0.7\ \mu\text{m}$  features (Kaluna 2015), which are present in CM meteorites that are spectrally dominated by Fe-rich phyllosilicates (Cloutis et al. 2011).

## 5. Conclusion

We have shown that pulsed laser irradiation of the two sets of minerals formed during aqueously alteration result in notable but varied spectral variations. Irradiation of Mg-rich lizardite results in little slope and albedo variations, but significant absorption band variations in which hydroxyl features are less affected by laser irradiation than Fe features. Irradiation of the Fe-rich sample (cronstedtite, pyrite and siderite) induces both spectral reddening and bluing, darkening, and absorption band suppression. SEM and TEM analyses of the Fe-rich assemblage revealed micron sized organic-like (CNO-rich) particles that appear to have been produced during irradiation and may be a new mechanism for spectral bluing. In addition to providing insight

into the potential compositional dependency of space weathering trends on volatile-rich asteroids, these data also indicate that space weathering may play an important role in the synthesis of organics on asteroid surfaces.

We would like to say mahalo nui to Karen Meech of the Institute for Astronomy, Jeff Taylor and Eric Hellebrand of HIGP, and Tina Carvalho of the PBRC for their contribution to and support of this work. Additionally, we would like to acknowledge Peter Eschbach at Oregon State University, and Karen Bustillo and Chengyu Song at the Molecular Foundry, Lawrence Berkeley Lab for their help with data collection. This work was supported by the National Aeronautics and Space Administration through the NASA Astrobiology Institute under Cooperative Agreement No. NNA04CC08A issued through the Office of Space Science, by NASA Grant No. NNX07A044G. Work was conducted at the Molecular Foundry (National Center of Electron Microscopy, Lawrence Berkeley National Lab) under Project 3688 (PI Ishii) and was supported by the Office of Science, Basic Energy Sciences, U.S. Department of Energy under Contract No. DE-AC02-05CH11231.

TABLE 1  
PREVIOUSLY PUBLISHED SPACE WEATHERING EXPERIMENTS ON VOLATILE-RICH CC METEORITES

Meteorite	Petrologic Grade	Slope Changes	Albedo Changes <sup>†</sup>	Method	Reference
Murchison (CM)	2.5-2.7 <sup>1,2</sup>	Blueing	Increase ( $< 0.5\mu\text{m}$ )	Laser	Matsuoka et al. (2015)
Murchison	2.5-2.7	NV	Decrease	He <sup>+</sup> Ion	Lantz et al. (2015b)
Murchison	2.5-2.7	NV	Increase ( $< 0.72\mu\text{m}$ )	Ar <sup>+</sup> Ion	Lantz et al. (2015b)
Murray (CM)	2.4-2.6 <sup>1,2</sup>	NQ	Decrease	H <sup>+</sup> Ion	Hapke (1966)
Mighei (CM)	2.3 <sup>3</sup>	Reddening	NQ	Laser	Moroz et al. (2004b)
Mighei	2.3	Blueing	Increase	He <sup>+</sup> Ion	Lantz et al. (2015a)
Tagish Lake (C <sup>§</sup> )	2.0 <sup>1,4</sup>	Blueing	Increase	Laser	Hiroi et al. (2004)
Tagish Lake	2.0	Reddening	Increase	He <sup>+</sup> Ion	Vernazza et al. (2013)
Tagish Lake	2.0	Blueing	Increase ( $< 1\mu\text{m}$ )	Ar <sup>+</sup> Ion	Vernazza et al. (2013)

NOTE.—NV: No variations, NQ: Not quantified. Petrologic grades derived by: <sup>1</sup>Rubin et al. (2007), <sup>2</sup>Trigo-Rodriguez et al. (2006), <sup>3</sup>Rubin (2007), <sup>4</sup>Gounelle et al. (2001). <sup>†</sup>When provided, wavelength region where brightening occurs is given, <sup>§</sup>A unique meteorite with affinities to CM and CI chondrites (Zolensky et al. 2002; Cloutis et al. 2012).

TABLE 2  
MICROPROBE RESULTS

Samples	SiO <sub>2</sub>	FeO	MgO	Al <sub>2</sub> O <sub>3</sub>	SO <sub>3</sub>	CO <sub>2</sub>	H <sub>2</sub> O <sup>‡</sup>
Olivine	41.13	9.51	49.26	—	—	—	—
Lizardite	39.34	1.68	39.71	0.22	—	—	12.91
<b>Fe-rich assemblage</b>							
Cronstedtite	17.38	76.32 <sup>a</sup>	—	—	0.09	—	9.79
Pyrite <sup>b</sup>	—	46.98	—	—	50.43	—	—
Pyrite <sup>bc</sup>	2.31	54.56	—	—	0.15	—	—
Siderite	—	60.68	—	—	0.03	37.77	—

NOTE.—Fractional abundances (wt.%) determined from electron microprobe analyses of the minerals used in this work. <sup>‡</sup> H<sub>2</sub>O abundance determined from stoichiometry. <sup>a</sup>Values reflect Fe<sub>2</sub>O<sub>3</sub> abundance. <sup>b</sup>Values reflect elemental Fe and S abundances. <sup>c</sup>Oxidized pyrite phase.

TABLE 3  
AVERAGE CHEMICAL COMPOSITIONS OF Fe-RICH ASSEMBLAGE MELTS

Sample	Facility	Si	Fe	S	C	N	O
FIB section 1	OSU	0.2±0.0	0.4±0.0	<i>nd</i>	66.1±2.1	17.0±0.7	16.2±0.6
FIB section 1 <sup>†</sup>	OSU	10.0±2.5	55.9±11.4	8.2±4.9	<i>nd</i>	<i>nd</i>	25.9±6.7
FIB section 1	NCEM	<i>nd</i>	<i>nd</i>	<i>nd</i>	80.9±1.0	11.1±1.5	80.0±1.4
FIB section 2	NCEM	<i>nd</i>	<i>nd</i>	<i>nd</i>	77.5±3.0	12.5±3.7	9.9 ±4.2
FIB section 2 <sup>‡</sup>	NCEM	5.3±3.8	45.5±7.8	4.3±6.7	15.2±2.0	4.4±3.1	25.3±2.3

NOTE.—Abundances are expressed in wt.%. <sup>†</sup> Average of two adjacent Fe melt regions <sup>‡</sup>Composition of rim surrounding carbon rich grain.

TABLE 4  
BEST FIT RADIATIVE TRANSFER MODEL ABUNDANCES

Irradiation Time	Nanophase Iron Abundance (wt%)	Microphase Carbon Abundance (wt%)	$\chi_{red}^2$
<b>Olivine<sup>a</sup></b>			
2.5 min	0.003	—	1.004
5.0 min	0.008	—	1.070
10 min	0.018	—	4.101
15 min	0.028	—	1.961
20 min	0.043	—	4.357
30 min	0.064	—	1.594
40 min	0.090	—	12.495
<b>Lizardite<sup>b</sup></b>			
2.5 min	0.000	—	0.357
5.0 min	0.001	—	0.423
10 min	0.002	—	0.938
15 min	0.002	—	2.239
20 min	0.004	—	1.297
30 min	0.006	—	2.629
40 min	0.003	—	7.543
<b>Fe-rich assemblage<sup>c</sup></b>			
2.5 min	0.078	0.028	1.646
5.0 min	0.162	0.053	1.646
10 min	0.223	0.103	1.646
15 min	0.190	0.122	1.646
20 min	0.155	0.189	3.241
30 min	0.175	0.312	3.241
40 min	0.000	0.417	3.241

NOTE.—Each of the models were produced using mean grain diameters of 37.5μm. <sup>a</sup>Olivine models were produced using a grain density ( $\rho$ ) of 3.32 g/cm<sup>3</sup> and an index of refraction ( $n$ ) of 1.64. <sup>b</sup>Lizardite models were produced using  $\rho$  = 2.55 g/cm<sup>3</sup> and  $n$  = 1.60. <sup>c</sup>Lizardite models were produced using  $\rho$  = 3.34 g/cm<sup>3</sup> and  $n$  = 1.72.



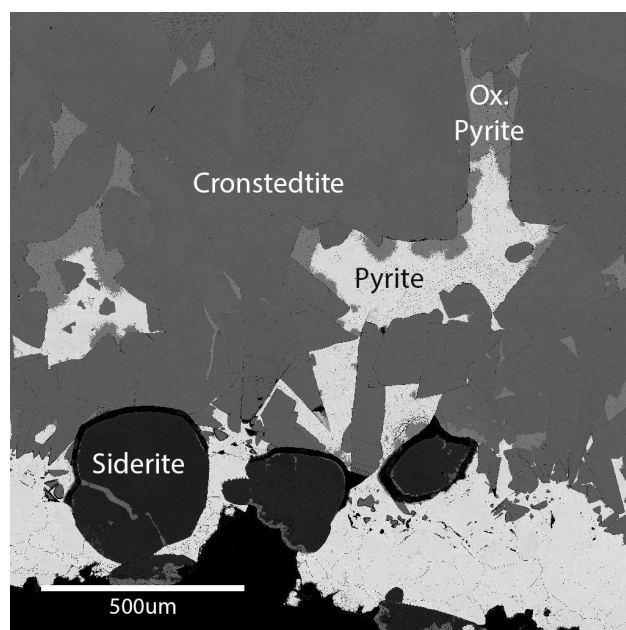


Fig. 1.— Secondary electron image of the mineral phases in the Fe-rich assemblage taken with the HIGP electron microprobe. In addition to cronstedtite, pyrite, and siderite, oxidized pyrite (ox. pyrite) was observed near pyrite and cronstedtite interfaces.

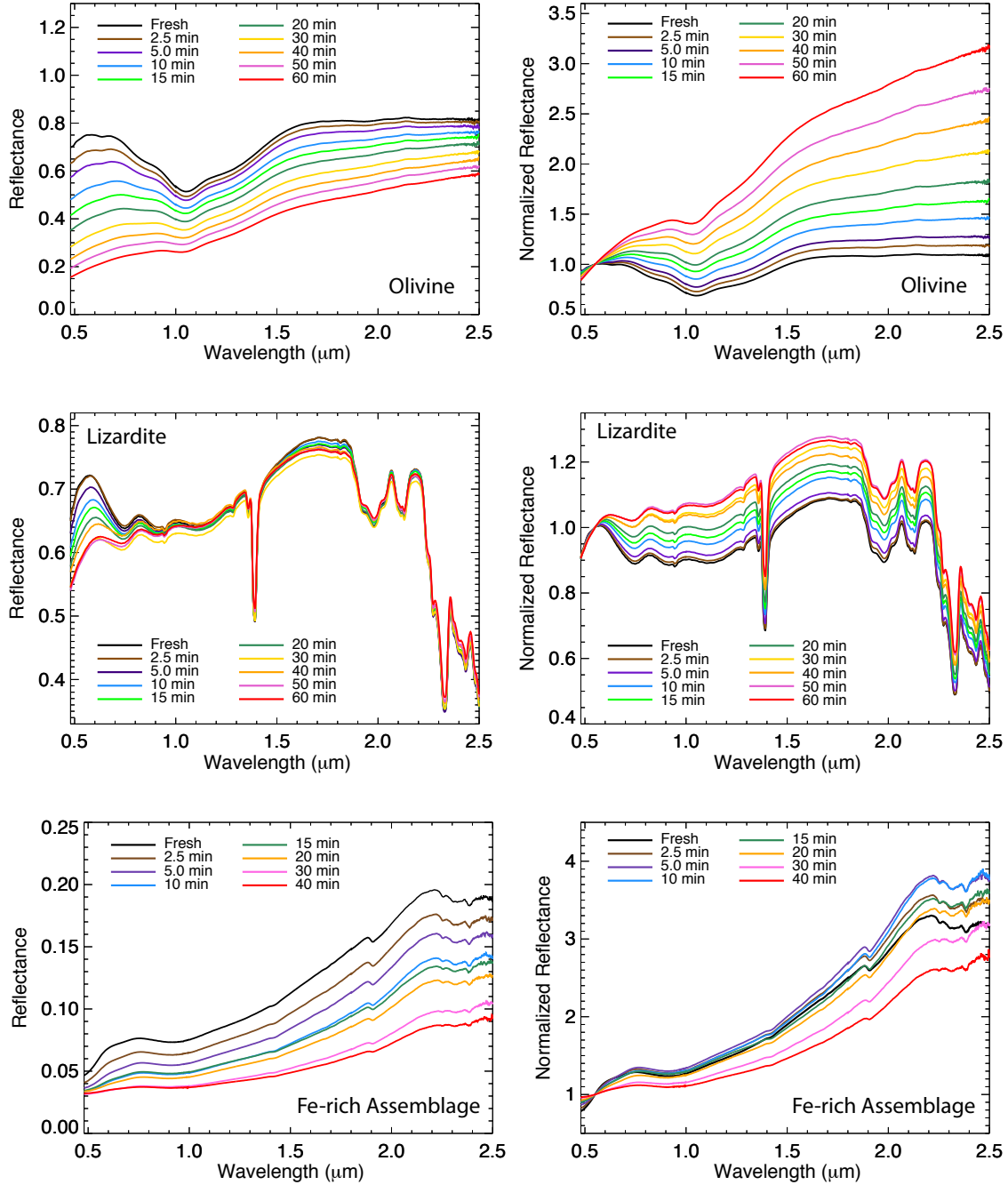


Fig. 2.— *Left:* Reflectance spectra for each sample as a function of laser irradiation time. The full 60 minute irradiation series are shown for olivine and lizardite, but due to sample loss in the Fe-rich samples, the total irradiation time was halted at 40 minutes. *Right:* Reflectance spectra normalized to 0.55  $\mu\text{m}$ .

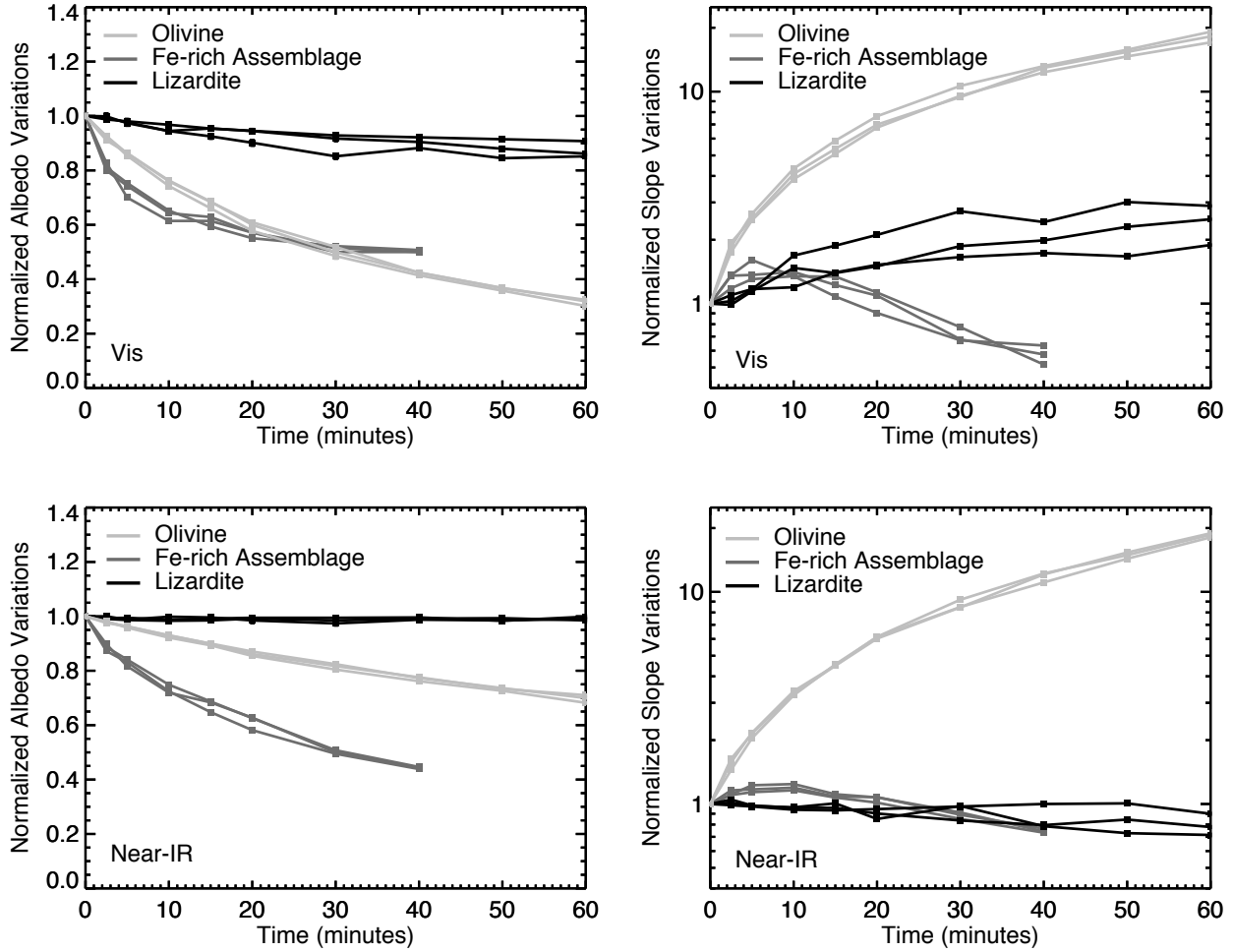


Fig. 3.— *Left:* Plots of relative slope changes in the visible (top) and NIR (bottom) for each experiment. Data have been normalized to the slope value of the fresh spectrum for each experiment. Visible slopes were measured using one continuum point in the visible when possible. *Right:* The relative changes in albedo for each experiment. Data have been normalized to the albedo value of the fresh spectrum for each experiment.

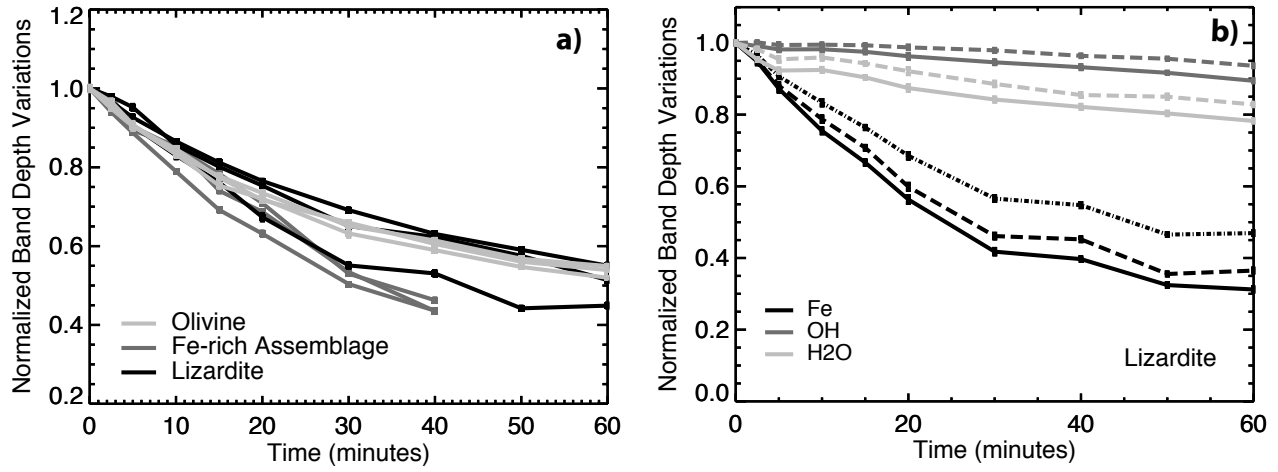


Fig. 4.— a) The variations in the olivine 1.05  $\mu\text{m}$ , lizardite 1.13  $\mu\text{m}$ , and Fe-rich assemblage  $\sim 2.4 \mu\text{m}$  band depths for each of the three experiments. The data have been normalized to the initial band depth values of the fresh, non-irradiated samples. b) The lizardite band depth variations for the  $\text{Fe}^{2+} \rightarrow \text{Fe}^{3+}$  0.75  $\mu\text{m}$  (solid), 0.92  $\mu\text{m}$  (dashed), 1.13  $\mu\text{m}$  (dashed-dot), the OH 1.4  $\mu\text{m}$  (solid) and 2.3  $\mu\text{m}$  (dashed) and the  $\text{H}_2\text{O}$  1.98  $\mu\text{m}$  (solid) and 2.13  $\mu\text{m}$  (dashed) features.

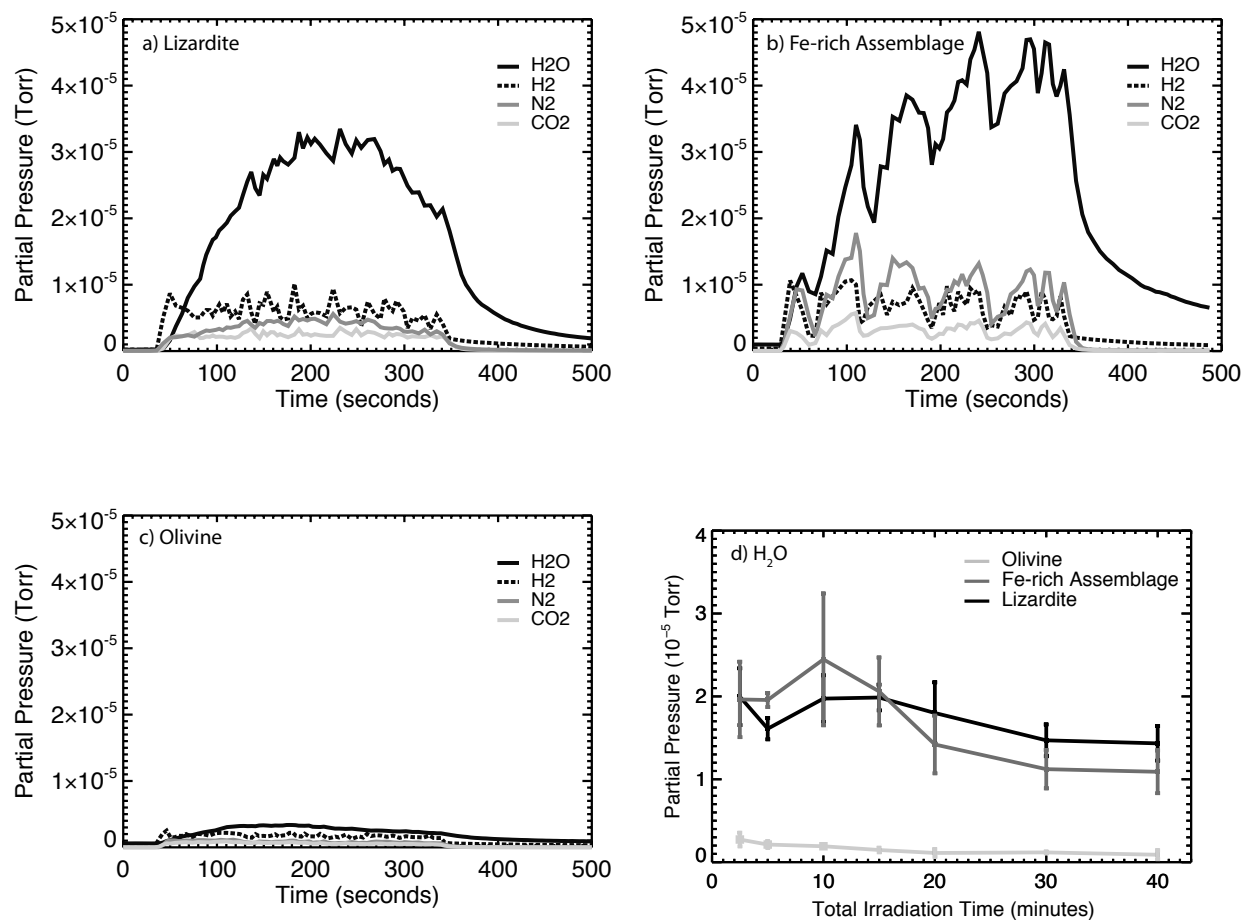


Fig. 5.—  $H_2O$  and trapped air constituents released during a 5 minute interval of laser irradiation on a) lizardite, b) the Fe-rich assemblage and c) olivine. *Note:* The peaks in figure b result from the laser spot nearing the edge of the sample. d) The mean partial pressures of  $H_2O$  released by the three minerals for all of the irradiation sets. Mean pressures and 1-sigma uncertainties were derived from the three sets of experiments conducted on each mineral/assemblage.

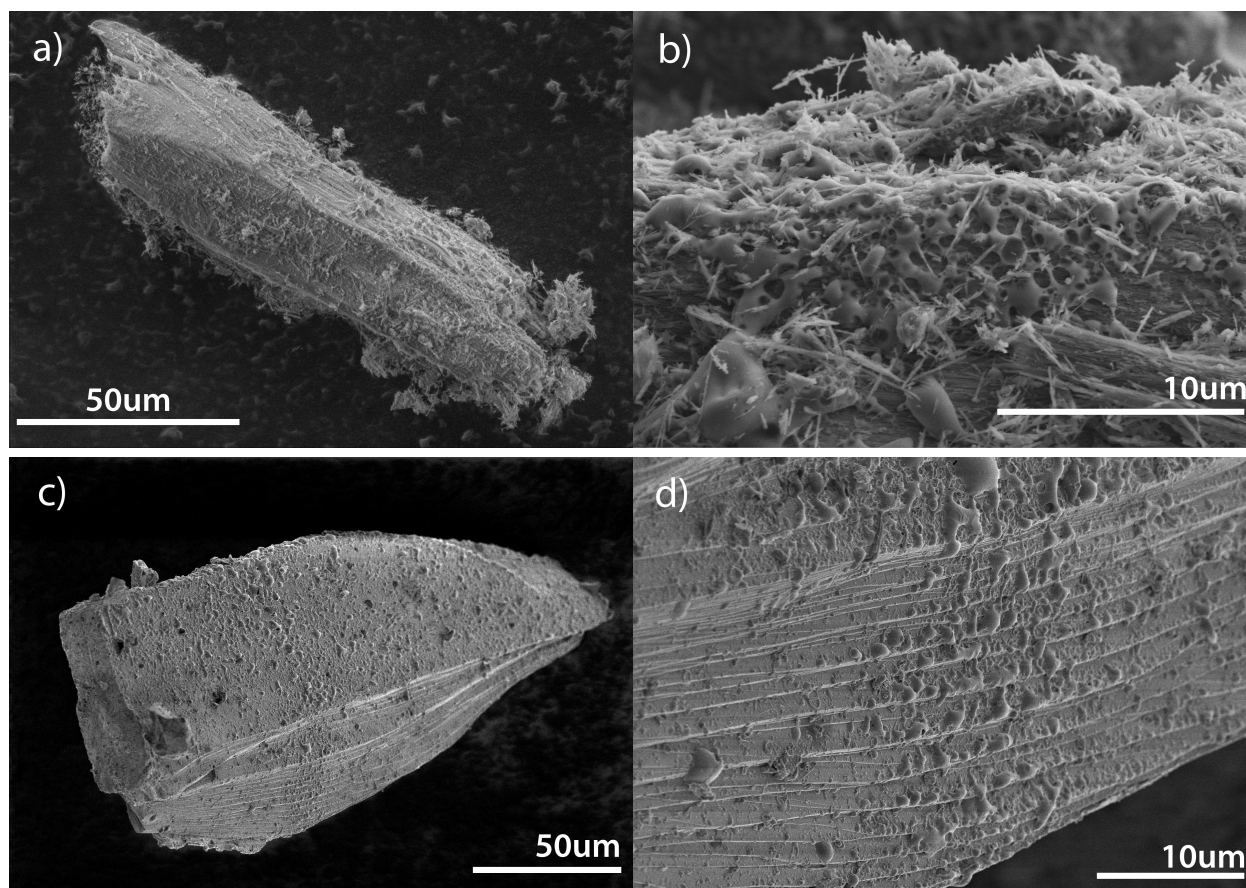


Fig. 6.— Secondary electron images of laser-irradiated lizardite and Fe-rich assemblage grains taken with the PBRC SEM. Images of 60 minute irradiated lizardite whole grain (a) and grain surface features (b). Images of a cronstedtite grain (c) and grain surface features (d) from a 40-minute irradiated Fe-rich assemblage sample.

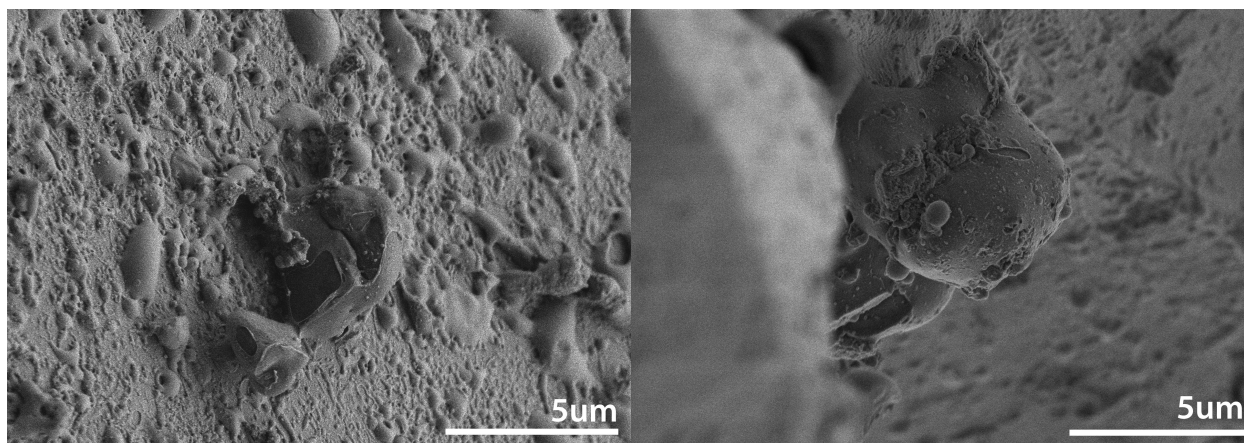


Fig. 7.— SE images of the two dark grains from the irradiated Fe-rich assemblage that were cut into FIB sections and analyzed with (S)TEM.



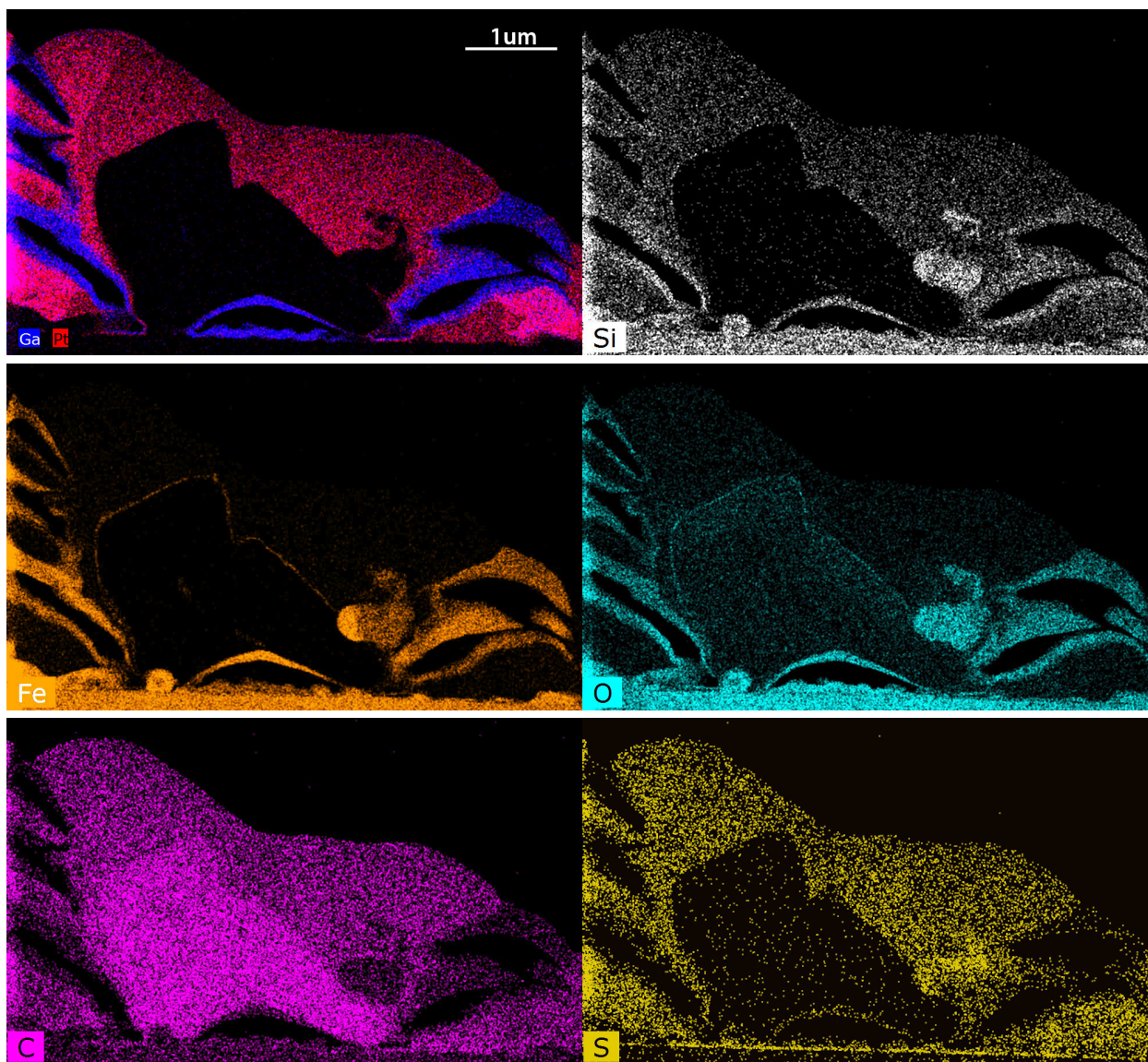


Fig. 8.— OSU Titan element maps of FIB section 1 created from an Fe-rich assemblage melt product. The Ga/Pt map references regions where materials used to create the FIB section are located and thus should be disregarded in other images. Analyses of the C-rich region shows the presence of C, N and O.



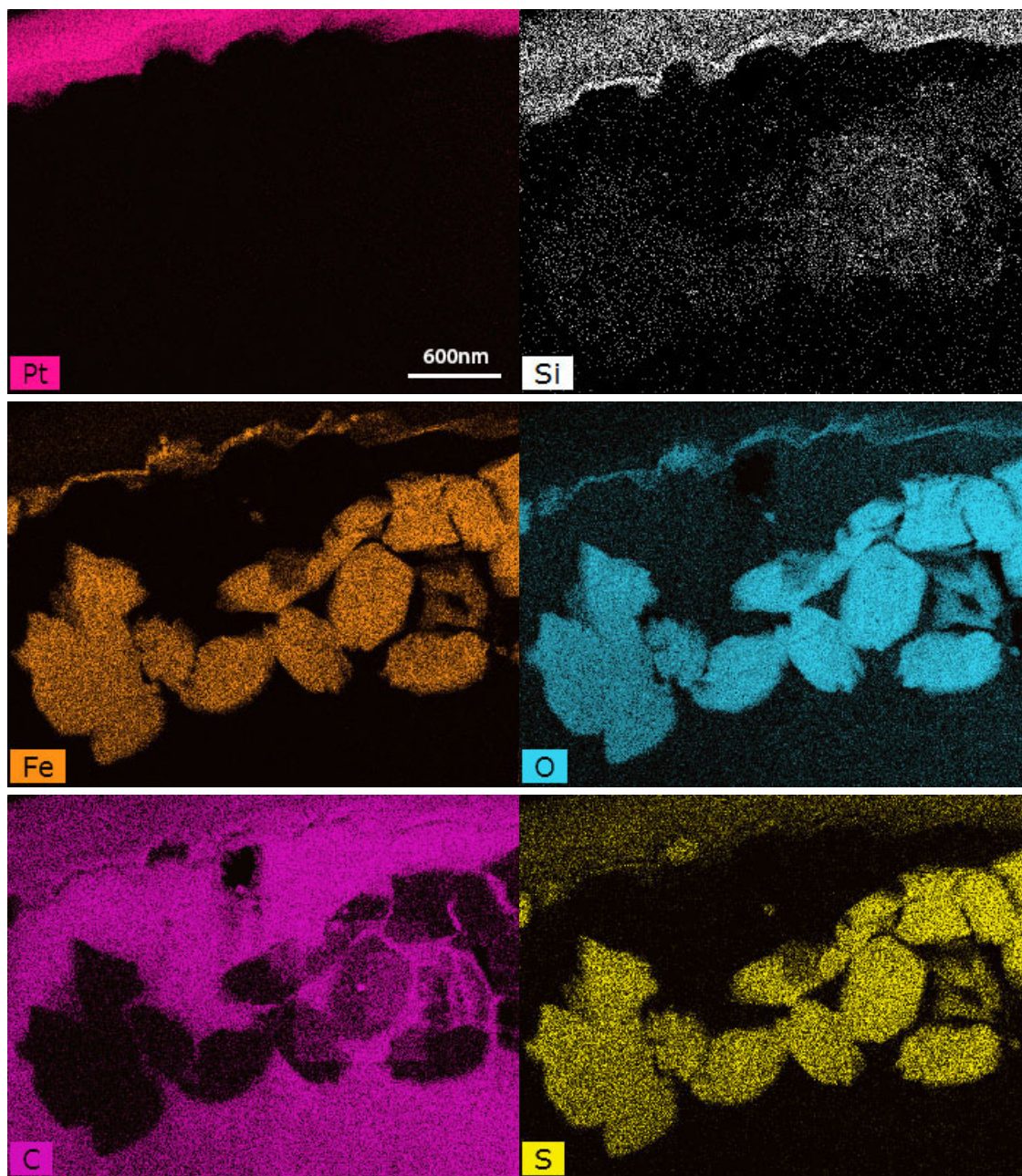


Fig. 9.— NCEM TitanX EDX maps of FIB section 2 created from an Fe-rich assemblage melt product. Oxidized pyrite grains are embedded in a carbon-rich melt grain. The Pt map references regions where materials used to create the FIB section are located and thus should be disregarded in the elemental maps.

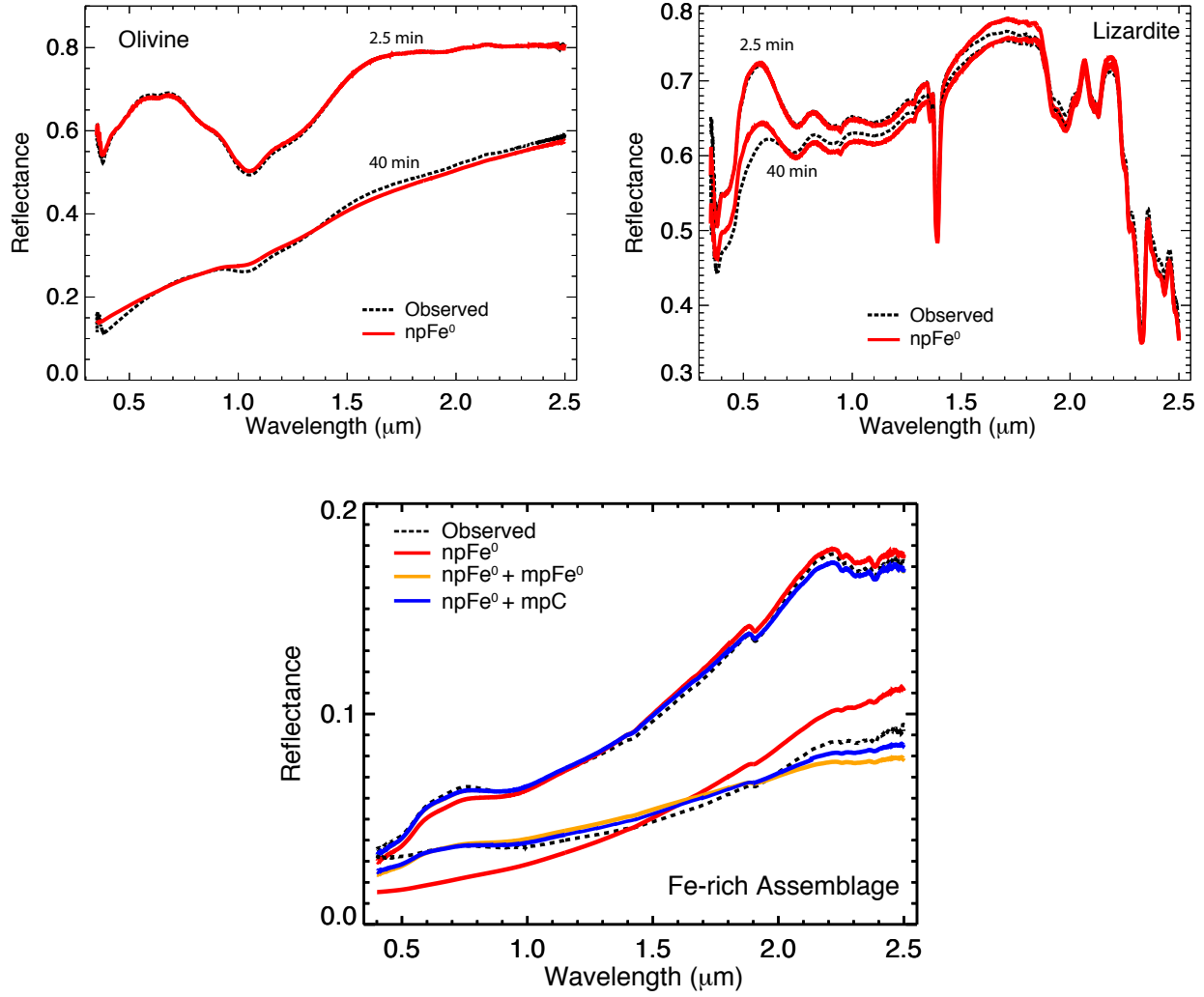


Fig. 10.— Observed olivine, lizardite and Fe-rich assemblage reflectance spectra and best fit radiative transfer models produced using the abundances given in Table 4. For clarity, only the 2.5 and 40 minute (total irradiation time) spectra and corresponding models are shown. *Note: the 2.5  $\text{npFe}^0$  and  $\mu\text{pC}$  model (blue) overlaps the  $\text{npFe}^0$  and  $\mu\text{pFe}^0$  model (orange).*

## REFERENCES

- Ammannito, E., De Sanctis, M. C., Ciarniello, M., Frigeri, A., Combe, J.-P., Carrozzo, F. G., Ehlmann, B. L., Marchi, S., McSween, H. Y., Raponi, A., Castillo-Rogez, J. C., Toplis, M. J., Tosi, F., Capaccioni, F., Capria, M. T., Fonte, S., Giardino, M., Jaumann, R., Longobardo, A., Joy, S. P., Magni, G., McCord, T. B., McFadden, L. A., Palomba, E., Pieters, C. M., Polanskey, C. A., Rayman, M. D., Raymond, C. A., Schenk, P., Zambon, F., & Russell, C. T. (2016). Distribution of Phyllosilicates on Ceres. In *Lunar and Planetary Science Conference* (p. 3020). volume 47 of *Lunar and Planetary Science Conference*.
- Bonner, W. A., Hall, H., Chow, G., Liang, Y., & Lemmon, R. M. (1985). The radiolysis and radioracemization of amino acids on clays. *Origins of Life*, 15, 103–114. doi:10.1007/BF01809492.
- Britt, D. T., Schelling, P. K., Consolmagno, G. J., & Bradley, T. (2014). Space Weathering on Volatile Rich Asteroids. In *Lunar and Planetary Science Conference* (p. 2067). volume 45 of *Lunar and Planetary Science Conference*.
- Brunetto, R., & Strazzulla, G. (2005). Elastic collisions in ion irradiation experiments: A mechanism for space weathering of silicates. *Icarus*, 179, 265–273. doi:10.1016/j.icarus.2005.07.001.
- Burbine, T. H., McCoy, T. J., Meibom, A., Gladman, B., & Keil, K. (2002). Meteoritic Parent Bodies: Their Number and Identification. *Asteroids III*, (pp. 653–667).
- Burns, R. G. (1993). *Mineralogical Applications of Crystal Field Theory*. Cambridge University Press.
- Bus, S. J., & Binzel, R. P. (2002). Phase II of the Small Main-Belt Asteroid Spectroscopic Survey. The Observations. *Icarus*, 158, 106–145. doi:10.1006/icar.2002.6857.
- Cahill, J. T. S., Blewett, D. T., Nguyen, N. V., Xu, K., Kirillov, O. A., Lawrence, S. J., Denevi, B. W., & Coman, E. I. (2012). Determination of iron metal optical constants: Implications for ultraviolet, visible, and near-infrared remote sensing of airless bodies. *Geophys. Res. Lett.*, 39, L10204. doi:10.1029/2012GL051630.
- Calvin, W. M., & King, T. V. V. (1997). Spectral characteristics of Fe-bearing phyllosilicates: Comparison to Orgueil (CI1), Murchison and Murray (CM2). *Meteoritics and Planetary Science*, 32, 693–701. doi:10.1111/j.1945-5100.1997.tb01554.x.
- Chapman, C. R. (2002). Cratering on Asteroids from Galileo and NEAR Shoemaker. *Asteroids III*, (pp. 315–329).
- Chyba, C., & Sagan, C. (1992). Endogenous production, exogenous delivery and impact-shock synthesis of organic molecules: an inventory for the origins of life. *Nature*, 355, 125–132. doi:10.1038/355125a0.
- Cloutis, E. A., Hudon, P., Hiroi, T., Gaffey, M. J., & Mann, P. (2011). Spectral reflectance properties of carbonaceous chondrites: 2. CM chondrites. *Icarus*, 216, 309–346. doi:10.1016/j.icarus.2011.09.009.
- Cloutis, E. A., Hudon, P., Hiroi, T., Gaffey, M. J., & Mann, P. (2012). Spectral reflectance properties of carbonaceous chondrites: 8. Other carbonaceous chondrites: CH, ungrouped, polymict, xenolithic inclusions, and R chondrites. *Icarus*, 221, 984–1001. doi:10.1016/j.icarus.2012.10.008.
- Combe, J.-P., McCord, T. B., Tosi, F., Ammannito, E., Carrozzo, F. G., De Sanctis, M. C., Raponi, A., Byrne, S., Landis, M. E., Hughson, K. H. et al. (2016). Detection of local h2o exposed at the surface of Ceres. *Science*, 353, aaf3010.
- Conel, J. E., & Nash, D. B. (1970). Spectral reflectance and albedo of Apollo 11 lunar samples: Effects of irradiation and vitrification and comparison with telescopic observations. *Geochimica et Cosmochimica Acta Supplement*, 1, 2013–2023.
- de Sanctis, M. C., Ammannito, E., Raponi, A., Marchi, S., McCord, T. B., McSween, H. Y., Capaccioni, F., Capria, M. T., Carrozzo, F. G., Ciarniello, M., Longobardo, A., Tosi, F., Fonte, S., Formisano, M., Frigeri, A., Giardino, M., Magni, G., Palomba, E., Turrini, D., Zambon, F., Combe, J.-P., Feldman, W., Jaumann, R., McFadden, L. A., Pieters, C. M., Prettyman, T., Toplis, M., Raymond, C. A., & Russell, C. T. (2015). Ammoniated phyllosilicates with a likely outer Solar System origin on (1) Ceres. *Nature*, 528, 241–244. doi:10.1038/nature16172.

- de Smit, E., & Weckhuysen, B. M. (2008). The renaissance of iron-based fischer-tropsch synthesis: on the multifaceted catalyst deactivation behaviour. *Chem. Soc. Rev.*, 37, 2758–2781. doi:10.1039/B805427D.
- Fornasier, S., Lantz, C., Barucci, M. A., & Lazzarin, M. (2014). Aqueous alteration on main belt primitive asteroids: Results from visible spectroscopy. *Icarus*, 233, 163–178. doi:10.1016/j.icarus.2014.01.040.
- Fornasier, S., Lantz, C., Perna, D., Campins, H., Barucci, M. A., & Nesvorný, D. (2016). Spectral variability on primitive asteroids of the Themis and Beagle families: Space weathering effects or parent body heterogeneity? *Icarus*, 269, 1–14. doi:10.1016/j.icarus.2016.01.002.
- Foti, G., Calcagno, L., Sheng, K. L., & Strazzulla, G. (1984). Micrometre-sized polymer layers synthesized by MeV ions impinging on frozen methane. *Nature*, 310, 126–128. doi:10.1038/310126a0.
- Gounelle, M., Zolensky, M. E., Tonui, E., & Mikouchi, T. (2001). Mineralogy of Tagish Lake, a Unique Type 2 Carbonaceous Chondrite. In *Lunar and Planetary Science Conference*. volume 32 of *Lunar and Planetary Science Conference*.
- Hapke, B. (1966). The Nature of the Lunar Surface. (pp. 141–154). Baltimore, Md: Johns Hopkins Univ. Press.
- Hapke, B. (2001). Space weathering from Mercury to the asteroid belt. *J. Geophys. Res.*, 106, 10039–10074. doi:10.1029/2000JE001338.
- Hirayama, K. (1918). Groups of asteroids probably of common origin. *AJ*, 31, 185–188. doi:10.1086/104299.
- Hiroi, T., Pieters, C. M., Rutherford, M. J., Zolensky, M. E., Sasaki, S., Ueda, Y., & Miyamoto, M. (2004). What are the P-type Asteroids Made Of? In S. Mackwell, & E. Stansbery (Eds.), *Lunar and Planetary Science Conference* (p. 1616). volume 35 of *Lunar and Planetary Inst. Technical Report*.
- Howard, K. T., Benedix, G. K., Bland, P. A., & Cressey, G. (2009). Modal mineralogy of CM2 chondrites by X-ray diffraction (PSD-XRD). Part 1: Total phyllosilicate abundance and the degree of aqueous alteration. *Geochimica et Cosmochimica Acta*, 73, 4576–4589. doi:10.1016/j.gca.2009.04.038.
- Howard, K. T., Benedix, G. K., Bland, P. A., & Cressey, G. (2011). Modal mineralogy of CM chondrites by X-ray diffraction (PSD-XRD): Part 2. Degree, nature and settings of aqueous alteration. *Geochimica et Cosmochimica Acta*, 75, 2735–2751. doi:10.1016/j.gca.2011.02.021.
- Hsieh, H. H. (2009). The Hawaii trails project: comet-hunting in the main asteroid belt. *A&A*, 505, 1297–1310. doi:10.1051/0004-6361/200912342.
- Ishiguro, M., Hiroi, T., Tholen, D. J., Sasaki, S., Ueda, Y., Nimura, T., Abe, M., Clark, B. E., Yamamoto, A., Yoshida, F. et al. (2007). Global mapping of the degree of space weathering on asteroid 25143 itokawa by hayabusa/amica observations. *Meteoritics & Planetary Science*, 42, 1791–1800.
- Ishii, H. A., Krot, A. N., Bradley, J. P., Keil, K., Nagashima, K., Teslich, N., Jacobsen, B., & Yin, Q. (2010). Discovery, mineral paragenesis, and origin of wadalite in a meteorite. *American Mineralogist*, 95, 440–448. URL: <http://ammin.geoscienceworld.org/content/95/4/440>. doi:10.2138/am.2010.3296.
- Jain, N., Bhattacharya, S., Chauhan, P., & Ajai (2012). Hyperspectral Study of Hydrous Magnesium Minerals (Serpentine) from Ultramafic Rocks Along the Rikhabdev Lineament, Rajasthan, India: As an Analogue for Hydrous Magnesium Minerals on Mars. In *Lunar and Planetary Science Conference* (p. 1474). volume 43 of *Lunar and Planetary Science Conference*.
- Jaumann, R., Stephan, K., Krohn, K., Matz, K.-D., Otto, K., Neumann, W., Kneissl, T., Schmedemann, N., Schroeder, S., Tosi, F., De Sanctis, M. C., Preusker, F., Buczkowski, D., Capaccioni, F., Carsenty, U., Elgner, S., von der Gathen, I., Gieber, T., Hiesinger, H., Hoffmann, M., Kersten, E., Li, J.-Y., McCord, T. B., McFadden, L., Motola, S., Nathues, A., Neesemann, A., Raymond, C., Roatsch, T., Russell, C. T., Schmidt, B., Schulzeck, F., Wagner, R., & Williams, D. A. (2016). Age-Dependent Morphological and Compositional Variations on Ceres. In *Lunar and Planetary Science Conference* (p. 1455). volume 47 of *Lunar and Planetary Science Conference*.

- Jedicke, R., Nesvorný, D., Whiteley, R., Ivezić, Ž., & Jurić, M. (2004). An age-colour relationship for main-belt S-complex asteroids. *Nature*, 429, 275–277. doi:10.1038/nature02578.
- Johnson, R. E., Lanzerotti, L. J., & Brown, W. L. (1984). Sputtering processes - Erosion and chemical change. *Advances in Space Research*, 4, 41–51. doi:10.1016/0273-1177(84)90007-3.
- Kaluna, H. M. (2015). *The evolution of water in carbonaceous main belt asteroids*. Ph.D. thesis University of Hawai'i at Manoa.
- Kaluna, H. M., Bus, S. J., Gillis-Davis, J. J., & Lucey, P. G. (2016a). The Composition and Evolution of Themis and Beagle Asteroids. In *Lunar and Planetary Science Conference* (p. 2892). volume 47 of *Lunar and Planetary Science Conference*.
- Kaluna, H. M., Masiero, J. R., & Meech, K. J. (2016b). Space weathering trends among carbonaceous asteroids. *Icarus*, 264, 62–71. doi:10.1016/j.icarus.2015.09.007.
- Kang, N., Schmidt, M. W., Poli, S., Franzolin, E., & Connolly, J. A. D. (2015). Melting of siderite to 20 GPa and thermodynamic properties of FeCO<sub>3</sub>-melt. *Chemical Geology*, 400, 34 – 43. doi:http://dx.doi.org/10.1016/j.chemgeo.2015.02.005.
- Keller, L. P., & McKay, D. S. (1993). Discovery of vapor deposits in the lunar regolith. *Science*, 261, 1305–1307. doi:10.1126/science.261.5126.1305.
- Keller, L. P., Rahman, Z., Hiroi, T., Sasaki, S., Noble, S. K., Horz, F., & Cintala, M. J. (2013). Asteroidal Space Weathering: The Major Role of FeS. In *Lunar and Planetary Science Conference* (p. 2404). volume 44 of *Lunar and Planetary Inst. Technical Report*.
- Küppers, M., O'Rourke, L., Bockelée-Morvan, D., Zakharov, V., Lee, S., von Allmen, P., Carry, B., Teyssier, D., Marston, A., Müller, T. et al. (2014). Localized sources of water vapour on the dwarf planet (1)[thinsp]ceres. *Nature*, 505, 525–527.
- Lantz, C., Brunetto, R., Barucci, M. A., Bachelet, C., Baklouti, D., Bourçois, J., Dartois, E., Duprat, J., Duret, P., Engrand, C., Godard, M., Ledu, D., Mivumbi, O., & Fornasier, S. (2015a). Ion irradiation of carbonaceous chondrites as a simulation of space weathering on C-complex asteroids. *European Planetary Science Congress 2015, held 27 September - 2 October, 2015 in Nantes, France*, 10, EPSC2015–138.
- Lantz, C., Brunetto, R., Barucci, M. A., Dartois, E., Duprat, J., Engrand, C., Godard, M., Ledu, D., & Quirico, E. (2015b). Ion irradiation of the Murchison meteorite: Visible to mid-infrared spectroscopic results. *A&A*, 577, A41. doi:10.1051/0004-6361/201425398.
- Lazzarin, M., Marchi, S., Moroz, L. V., Brunetto, R., Magrin, S., Paolicchi, P., & Strazzulla, G. (2006). Space Weathering in the Main Asteroid Belt: The Big Picture. *ApJ*, 647, L179–L182. doi:10.1086/507448.
- Lebofsky, L. A., Feierberg, M. A., Tokunaga, A. T., Larson, H. P., & Johnson, J. R. (1981). The 1.7- to 4.2-micron spectrum of asteroid 1 Ceres - Evidence for structural water in clay minerals. *Icarus*, 48, 453–459. doi:10.1016/0019-1035(81)90055-5.
- Lucey, P. G., & Riner, M. A. (2011). The optical effects of small iron particles that darken but do not redden: Evidence of intense space weathering on Mercury. *Icarus*, 212, 451–462. doi:10.1016/j.icarus.2011.01.022.
- Markwardt, C. B. (2009). Non-linear Least-squares Fitting in IDL with MPFIT. In D. A. Bohlen-der, D. Durand, & P. Dowler (Eds.), *Astronomical Data Analysis Software and Systems XVIII* (p. 251). volume 411 of *Astronomical Society of the Pacific Conference Series*.
- Matsuoka, M., Nakamura, T., Kimura, Y., Hiroi, T., Nakamura, R., Okumura, S., & Sasaki, S. (2015). Pulse-laser irradiation experiments of Murchison CM2 chondrite for reproducing space weathering on C-type asteroids. *Icarus*, 254, 135–143. doi:10.1016/j.icarus.2015.02.029.
- McDonald, G. D., Whited, L. J., DeRuiter, C., Khare, B. N., Patnaik, A., & Sagan, C. (1996). Production and Chemical Analysis of Cometary Ice Tholins. *Icarus*, 122, 107–117. doi:10.1006/icar.1996.0112.
- McKay, D. S., Heiken, G. H., Basu, A., Blanford, G., Simon, S., Reedy, R., French, B. M., & Papike, J.

- (1991). Lunar Sourcebook. chapter The Lunar Regolith. (pp. 285–356). Cambridge University Press.
- Moroz, L., Baratta, G., Strazzulla, G., Starukhina, L., Dotto, E., Barucci, M. A., Arnold, G., & Distefano, E. (2004a). Optical alteration of complex organics induced by ion irradiation: 1. Laboratory experiments suggest unusual space weathering trend. *Icarus*, 170, 214–228. doi:10.1016/j.icarus.2004.02.003.
- Moroz, L. V., Arnold, G., Korochantsev, A. V., & Wäsch, R. (1998). Natural Solid Bitumens as Possible Analogs for Cometary and Asteroid Organics: 1. Reflectance Spectroscopy of Pure Bitumens. *Icarus*, 134, 253–268. doi:10.1006/icar.1998.5955.
- Moroz, L. V., Hiroi, T., Shingareva, T. V., Basilevsky, A. T., Fisenko, A. V., Semjonova, L. F., & Pieters, C. M. (2004b). Reflectance Spectra of CM2 Chondrite Mighei Irradiated with Pulsed Laser and Implications for Low-Albedo Asteroids and Martian Moons. In S. Mackwell, & E. Stansbery (Eds.), *Lunar and Planetary Science Conference* (p. 1279). volume 35 of *Lunar and Planetary Science Conference*.
- Nesvorný, D., Bottke, W. F., Vokrouhlický, D., Sykes, M., Lien, D. J., & Stansberry, J. (2008). Origin of the Near-Ecliptic Circumsolar Dust Band. *ApJ*, 679, L143–L146. doi:10.1086/588841.
- Nesvorný, D., Jedicke, R., Whiteley, R. J., & Ivezić, Ž. (2005). Evidence for asteroid space weathering from the Sloan Digital Sky Survey. *Icarus*, 173, 132–152. doi:10.1016/j.icarus.2004.07.026.
- Noguchi, T., Nakamura, T., Kimura, M., Zolensky, M. E., Tanaka, M., Hashimoto, T., Konno, M., Nakato, A., Ogami, T., Fujimura, A., Abe, M., Yada, T., Mukai, T., Ueno, M., Okada, T., Shirai, K., Ishibashi, Y., & Okazaki, R. (2011). Incipient Space Weathering Observed on the Surface of Itokawa Dust Particles. *Science*, 333, 1121. doi:10.1126/science.1207794.
- Noguchi, T., Yabuta, H., Itoh, S., Sakamoto, N., Mitunari, T., Okubo, A., Okazaki, R., Nakamura, T., Tachibana, S., Terada, K., Ebihara, M., Imae, N., Kimura, M., & Nagahara, H. (2016). Early Stage of Aqueous Alteration and Interaction Between Inorganic and Organic Materials in Cometary Bodies: Insights from Antarctic Micrometeorites. In *Lunar and Planetary Science Conference* (p. 1426). volume 47 of *Lunar and Planetary Science Conference*.
- Novaković, B., Hsieh, H. H., & Cellino, A. (2012). P/2006 VW<sub>139</sub>: a main-belt comet born in an asteroid collision? *MNRAS*, 424, 1432–1441. doi:10.1111/j.1365-2966.2012.21329.x.
- Ogliore, R. C., & Dobrica, E. (2015). Space-Weathering Features on Two Hayabusa Particles. In *Lunar and Planetary Science Conference* (p. 1631). volume 46 of *Lunar and Planetary Science Conference*.
- Pieters, C. M., Taylor, L. A., Noble, S. K., Keller, L. P., Hapke, B., Morris, R. V., Allen, C. C., McKay, D. S., & Wentworth, S. (2000). Space weathering on airless bodies: Resolving a mystery with lunar samples. *Meteoritics and Planetary Science*, 35, 1101–1107. doi:10.1111/j.1945-5100.2000.tb01496.x.
- Pizzarello, S., & Williams, L. B. (2012). Ammonia in the Early Solar System: An Account from Carbonaceous Meteorites. *ApJ*, 749, 161. doi:10.1088/0004-637X/749/2/161.
- Rivkin, A. S., Howell, E. S., Vilas, F., & Lebofsky, L. A. (2002). Hydrated Minerals on Asteroids: The Astronomical Record. *Asteroids III*, (pp. 235–253).
- Rouleau, F., & Martin, P. G. (1991). Shape and clustering effects on the optical properties of amorphous carbon. *ApJ*, 377, 526–540. doi:10.1086/170382.
- Rubin, A. E. (2007). Progressive Alteration of CM Chondrites: Effects on Refractory Inclusions. In *Lunar and Planetary Science Conference* (p. 1230). volume 38 of *Lunar and Planetary Science Conference*.
- Rubin, A. E., Trigo-Rodríguez, J. M., Huber, H., & Wasson, J. T. (2007). Progressive aqueous alteration of CM carbonaceous chondrites. *Geochim. Cosmochim. Acta*, 71, 2361–2382. doi:10.1016/j.gca.2007.02.008.
- Russell, C., & Raymond, C. (2011). The dawn mission to vesta and ceres. *Space Science Reviews*, 163, 3–23.
- Sasaki, S., Kurahashi, E., Yamanaka, C., & Nakamura, K. (2003). Laboratory simulation of space weathering: Changes of optical properties and TEM/ESR



- confirmation of nanophase metallic iron. *Advances in Space Research*, 31, 2537–2542. doi:10.1016/S0273-1177(03)00575-1.
- Sasaki, S., Nakamura, K., Hamabe, Y., Kurahashi, E., & Hiroi, T. (2001). Production of iron nanoparticles by laser irradiation in a simulation of lunar-like space weathering. *Nature*, 410, 555–557.
- Simakov, M. B., & Kuzicheva, E. A. (2005). Abiogenic photochemical synthesis on surface of meteorites and other small space bodies. *Advances in Space Research*, 36, 190–194. doi:10.1016/j.asr.2004.12.064.
- Strazzulla, G., & Johnson, R. E. (1991). Irradiation effects on comets and cometary debris. In R. L. Newburn, Jr., M. Neugebauer, & J. Rahe (Eds.), *IAU Colloq. 116: Comets in the post-Halley era* (pp. 243–275). volume 167 of *Astrophysics and Space Science Library*.
- Trigo-Rodriguez, J. M., Rubin, A. E., & Wasson, J. T. (2006). Non-nebular origin of dark mantles around chondrules and inclusions in CM chondrites. *Geochim. Cosmochim. Acta*, 70, 1271–1290. doi:10.1016/j.gca.2005.11.009.
- Vernazza, P., Fulvio, D., Brunetto, R., Emery, J. P., Dukes, C. A., Cipriani, F., Witasse, O., Schaible, M. J., Zanda, B., Strazzulla, G., & Baragiola, R. A. (2013). Paucity of Tagish Lake-like parent bodies in the Asteroid Belt and among Jupiter Trojans. *Icarus*, 225, 517–525. doi:10.1016/j.icarus.2013.04.019.
- Vilas, F., & Gaffey, M. J. (1989). Phyllosilicate absorption features in main-belt and outer-belt asteroid reflectance spectra. *Science*, 246, 790–792. doi:10.1126/science.246.4931.790.
- Yamada, M., Sasaki, S., Nagahara, H., Fujiwara, A., Hasegawa, S., Yano, H., Hiroi, T., Ohashi, H., & Otake, H. (1999). Simulation of space weathering of planet-forming materials: Nanosecond pulse laser irradiation and proton implantation on olivine and pyroxene samples. *Earth, Planets, and Space*, 51, 1255–1265. doi:10.1186/BF03351599.
- Zolensky, M. E., Nakamura, K., Gounelle, M., Mikouchi, T., Kasama, T., Tachikawa, O., & Tonui, E. (2002). Mineralogy of Tagish Lake: An ungrouped type 2 carbonaceous chondrite. *Meteoritics and Planetary Science*, 37, 737–761. doi:10.1111/j.1945-5100.2002.tb00852.x.